

# The Magellan Uniform Survey of Damped Lyman $\alpha$ Systems I: Cosmic Metallicity Evolution<sup>★</sup>

Regina A. Jorgenson<sup>1,2,†</sup>, Michael T. Murphy<sup>3</sup>, Rodger Thompson<sup>4</sup>

<sup>1</sup> *Institute for Astronomy, University of Hawai'i, 2680 Woodlawn Dr, Honolulu, HI 96822, USA*

<sup>2</sup> *Institute of Astronomy, University of Cambridge, Madingley Road, Cambridge, CB3 0HA, UK*

<sup>3</sup> *Centre for Astrophysics and Supercomputing, Swinburne University of Technology, Hawthorn, Melbourne, VIC 3122, Australia*

<sup>4</sup> *Steward Observatory, University of Arizona, Tucson, AZ 85721, USA*

Submitted 30 October 2021.

## ABSTRACT

We present the chemical abundance measurements of the first large, medium-resolution, uniformly selected damped Lyman- $\alpha$  system (DLA) survey. The sample contains 99 DLAs towards 89 quasars selected from the SDSS DR5 DLA sample in a uniform way. We analyze the metallicities and kinematic diagnostics, including the velocity width of 90% of the optical depth,  $\Delta v_{90}$ , and the equivalent widths of the Si II  $\lambda 1526$  ( $W_{\lambda 1526}$ ), C IV  $\lambda 1548$  and Mg II  $\lambda 2796$  transitions. To avoid strong line-saturation effects on the metallicities measured in medium-resolution spectra (FWHM  $\sim 71$  km s<sup>-1</sup>), we derived metallicities from metal transitions which absorbed at most 35% of the quasar continuum flux. We find the evolution in cosmic mean metallicity of the sample,  $\langle Z \rangle = (-0.04 \pm 0.13)z - (1.06 \pm 0.36)$ , consistent with no evolution over the redshift range  $z \sim [2.2, 4.4]$ , but note that the majority of our sample falls at  $z \sim [2.2, 3.5]$ . The apparent lack of metallicity evolution with redshift is also seen in a lack of evolution in the median  $\Delta v_{90}$  and  $W_{\lambda 1526}$  values. While this result may seem to conflict with other large surveys that have detected significant metallicity evolution, such as Rafelski et al. (2012) who found  $\langle Z \rangle = (-0.22 \pm 0.03)z - (0.65 \pm 0.09)$  over  $z \sim [0, 5]$ , several tests show that these surveys are not inconsistent with our new result. However, over the smaller redshift range covered by our uniformly-selected sample, the true evolution of the cosmic mean metallicity in DLAs may be somewhat flatter than the Rafelski et al. (2012) estimate.

**Key words:** galaxies: evolution – galaxies: high-redshift – galaxies: intergalactic medium – galaxies: quasars: absorption lines

## 1 INTRODUCTION

The damped Lyman- $\alpha$  systems (DLAs), quasar absorption line systems having neutral gas columns of  $N_{\text{HI}} \geq 2 \times 10^{20}$  cm<sup>-2</sup>, represent a unique laboratory for understanding the conversion of neutral gas into stars at high redshift. Dominating the neutral gas mass density between  $z=[0, 5]$  (Wolfe et al. 2005), the DLAs are believed to host the reservoirs of neutral gas for star formation across cosmic time. However, the exact connection between DLAs and high redshift star formation remains elusive.

One of the most compelling pieces of evidence for a connection between DLAs and high redshift star formation is the evolution of the cosmological mean metallicity (e.g. Vladilo et al. (2000);

Vladilo (2002); Prochaska et al. (2003a); Kulkarni et al. (2005, 2007, 2010); Rafelski et al. (2012)). This quantity, denoted by  $\langle Z \rangle$  and defined by Lanzetta et al. (1995) as  $\Omega_{\text{metals}}/\Omega_{\text{gas}}$ , describes the amount of metals contained in the gas of DLAs. Given that DLAs trace the neutral gas mass density of the Universe over cosmic time and that they are believed to be the neutral gas reservoirs for star formation, a natural consequence of this picture implies that the cosmic metallicity of DLAs should increase with time as subsequent generations of supernovae enrich the gas. Therefore, tracing this metallicity evolution to high redshifts can provide important constraints on models of galaxy formation and evolution (Davé et al. 2011; Fumagalli et al. 2011; Cen 2012).

Contrary to expectations, initial studies (e. g. Pettini et al. (1999)) found no apparent evolution in the cosmic metallicity of DLA gas. Pettini et al. (1999) analyzed 40 DLAs in the redshift range  $z \sim [0.5, 3.5]$  and reported no evidence for an increase of the column density-weighted metallicity below  $z \sim 1.5$  as compared

<sup>★</sup> This paper includes data gathered with the 6.5 meter Magellan Telescopes located at Las Campanas Observatory, Chile.

<sup>†</sup> NSF Astronomy and Astrophysics Postdoctoral Fellow; raj@ifhawaii.edu

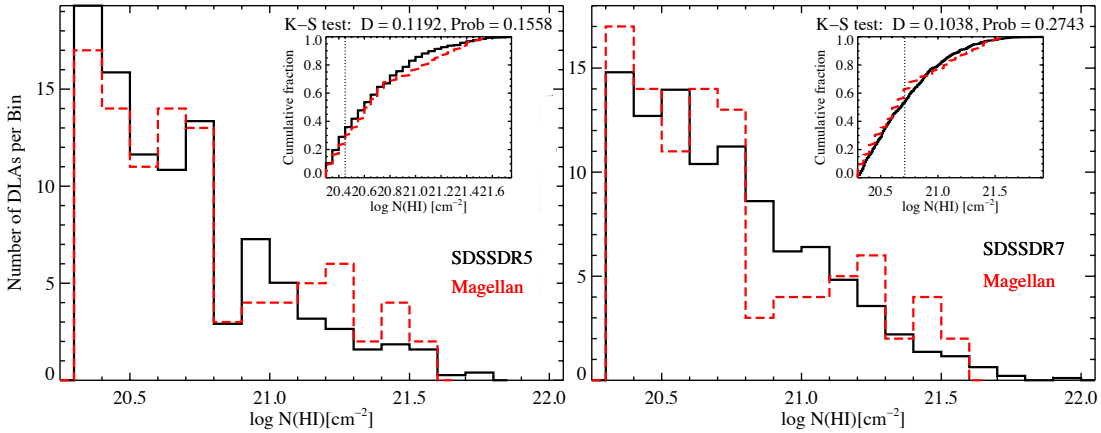


**Figure 1.**  $N_{\text{HI}}$  histogram comparing the Magellan sample (red dashed line) with the scaled SDSS DR5 (Prochaska et al. 2005) distribution (black), left, and with the scaled SDSS DR7 (Noterdaeme et al. 2009) distribution, right. A K-S test indicates the probability they are drawn from the same parent population is  $P_{KS} = 0.16$  and  $P_{KS} = 0.27$ , respectively.

with higher redshifts. They noted that this conflicts with the peak of the comoving star formation rate density that reaches a maximum between  $z = 1 - 2$ . Pettini et al. (1999) concluded that the apparent lack of evolution in metallicity could not be reconciled with the idea that DLAs fuelled the bulk of cosmic star formation at these epochs. If, indeed, DLAs are an unbiased probe of this gas cycle, the cosmic mean metallicity of DLAs *should* show a corresponding increase in step with the increase in the comoving star formation rate density of the Universe.

However, as samples grew in size, evolution in the cosmic mean metallicity of DLAs *was* detected: first, by Prochaska et al. (2003a), who found an evolution of  $-0.26 \pm 0.07$  dex per unit redshift in a sample of 125 DLAs over the redshift range  $z = [0.5, 5]$ . This evolution was confirmed in studies by Kulkarni et al. (2005, 2007, 2010). Recently, the Prochaska et al. (2003a) sample was expanded by Rafelski et al. (2012), who obtained medium and high-resolution follow-up of 30 high- $z$  ( $z > 4$ ) DLAs. With an increased sample size of 242 DLAs, Rafelski et al. (2012) detected a  $6\sigma$  significant evolution in cosmic metallicity of  $-0.22 \pm 0.03$  dex per unit redshift from  $z = 0.09 - 5.06$ . This apparent detection of evolution in metallicity over cosmic time may be important evidence linking DLA gas with star formation.

With the aim of further elucidating the connection between DLAs and star formation, we recently completed a large, medium-resolution, uniformly selected survey of DLAs. Our main motivation was to quantify the covering fraction of molecular hydrogen – an important link between neutral gas and star formation – so we took advantage of the exceptional blue throughput of the Magellan/MagE spectrograph in order to search for the redshifted UV Lyman and Werner band  $\text{H}_2$  lines. Our sample consists of 99 DLAs towards 89 quasars, selected from the SDSS DR5 catalog in a uniform way, i.e. including all DLAs visible from the Magellan site with  $i$ -band magnitude  $\leq 19$ . For convenience we will refer to this new sample of DLA spectra as the ‘Magellan sample’ even though it comprises spectra from other telescopes as well (for some targets missed due to bad weather). Given the importance of understanding the metallicity evolution of DLAs and the effects of any potential biases in previous samples, we present in this paper the results of

the metallicity analysis of the Magellan sample. We present the results of the search for  $\text{H}_2$  in a second paper (Jorgenson et al. 2013b).

This paper is organized as follows. We discuss our sample selection, observational details, and data reduction in § 2 while § 3 contains a description of our procedure for measuring the metal-line column densities in each DLA. In § 4 we discuss the evidence for metallicity evolution. An analysis of other DLA diagnostics is presented in § 5. Finally, we summarize the results and conclude in § 6.

## 2 DATA & METHODOLOGY

### 2.1 Sample Selection

In constructing the DLA sample presented in this paper, our primary goal was to determine the true covering factor and fraction of  $\text{H}_2$  in DLAs. To achieve this goal, we created a DLA sample drawn with uniform selection criteria from the SDSS DR5 DLA sample of Prochaska et al. (2005) with the aim of minimizing possible biases. We used just 3 simple selection criteria: 1) the target quasar had to be visible from the Magellan site ( $\text{dec} \leq 15^\circ$ ), 2) the redshift of the DLA was required to be  $z_{\text{abs}} \geq 2.2$ , such that the Lyman and Werner band molecular line region fell at  $\lambda^{\text{observed}} \geq 3200\text{\AA}$  and was observable from the ground and 3) the target quasar had an  $i$ -band magnitude of  $i \leq 19$ , such that we created a reasonably sized sample that could be observed spectroscopically at moderate resolution with non-prohibitive amounts of telescope time. This selection produced a total of 106 DLAs, towards 97 quasars.

The resulting DLA sample, referred to here as the ‘Magellan sample,’ is unique in the sense that it is the only large, uniformly selected DLA survey with medium-resolution (or higher) spectra allowing for metallicity measurements. Because our sample was taken directly from the SDSS in an unbiased way, the H I column density distribution,  $f(N_{\text{HI}})$ , is fairly well matched to that of the SDSS DR5 survey (see Figure 1, left). A two sided Kolmogorov-Smirnov (K-S) test shows that the probability of our sample and

the SDSS DR5 (left) and SDSS DR7 (right) (Noterdaeme et al. 2009) sample to be drawn from the same parent population is  $P_{KS} = 0.16$ , and  $P_{KS} = 0.27$ , respectively. While our sample was designed to be as unbiased as possible, we note that, like any other DLA sample created from the SDSS survey, our sample will contain any of the biases inherent in the SDSS sample. While dust-bias of the magnitude-limited SDSS sample is likely not a major issue (see, for example, Ellison et al. (2001); Murphy & Liske (2004); Jorgenson et al. (2006); Vladilo et al. (2008); Frank & Péroux (2010); Khare et al. (2012)), it is more difficult to assess how other biases, such as those created by color selection (i.e. Richards et al. (2001); Worseck & Prochaska (2011)), may affect the results. For example, Worseck & Prochaska (2011) showed that a certain population of quasars is systematically missed in the SDSS selection because of overlap with the stellar locus in color space. While this may be an important issue, it is outside the scope of the current paper and we will not consider the implications of biases in the SDSS further.

In contrast with other surveys that heavily relied on archival and previously published data to create samples used to measure the  $H_2$  fraction (Ledoux et al. 2006) or the cosmic mean metallicity (Rafelski et al. 2012; Prochaska et al. 2003a) of DLAs, the sample presented here was created *a priori* to be an  $H_2$ -blind and independent representation of the DLA population without regard to  $N(\text{HI})$ , metallicity, kinematics, or any other property of the DLA system. While we were unable to obtain spectra of 10 sample DLAs due to bad weather (discussed in detail in § 2.2), these ‘missing’ DLAs should not add any additional bias to the sample. Therefore, we argue that our sample is a less biased sample than those contained in previously published surveys and as a result, represents an important check on the results of those inhomogeneously created samples. We discuss the issue of potential sample biases in greater detail in § 4.2.

## 2.2 Data Acquisition and Reduction

Spectra were observed primarily during four observing runs during December 2008, and January, June and July of 2009 with the Magellan Echellette (MagE) Spectrometer on the Magellan II Clay telescope at Las Campanas Observatory (Marshall et al. 2008). MagE was chosen as the best instrument for this survey primarily because of its excellent blue sensitivity, required for observing the redshifted Lyman and Werner band molecular hydrogen transitions that fall in the restframe UV. In addition, the moderate spectral resolution ( $\sim 71 \text{ km s}^{-1}$ ) and large continuous wavelength coverage of 3100 Å to 1 micron allowed for a relatively large survey in a reasonable amount of time with excellent wavelength coverage of each DLA. All of the MagE spectra were taken with a  $1''.0$  slit giving a FWHM resolution of  $\approx 71 \text{ km s}^{-1}$ . Exposure times ranged from 1200 to 8100 seconds resulting in a median S/N in the optimally extracted spectra of  $S/N \sim 30$  per resolution element.

Unfortunately, due to bad weather, 15 sample quasars were not observed with MagE. Several of these ‘missed’ targets were later obtained with the X-Shooter spectrograph (D’Odorico et al. 2004). In total 8 target DLAs towards 7 quasars were obtained with X-Shooter. These spectra were observed with a  $1''.0$  slit giving a FWHM resolution of  $\approx 59 \text{ km s}^{-1}$ .

In addition, if high resolution echelle spectra of a sample quasar already existed in the Keck/HIRES (Vogt et al. 1994) and/or VLT/UVES (Dekker et al. 2000) archives, we did not re-observe it with MagE or X-Shooter (though there are some exceptions). Exist-

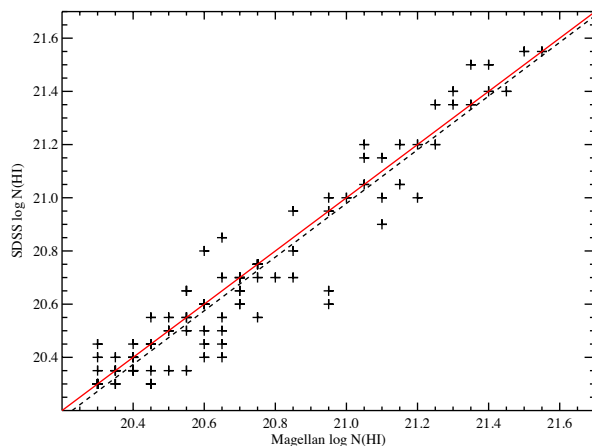


**Figure 2.** A comparison of the SDSS-derived  $N_{\text{HI}}$  measurements with those of the Magellan sample. The red solid line indicates slope = 1, while the black dashed line is a least squares best-fit to the data with slope = 1.009.

ing high-resolution spectra were obtained from the archives of the VLT/UVES and Keck/HIRES spectrographs for 21 and 8 DLAs, respectively. These spectra were typically observed with a slit producing a resolution of  $\approx 7 \text{ km s}^{-1}$ . Details of the total exposure time and instrument used for each target are given in Table 1. Note that if a target was observed with two different instruments it is listed in Table 1 twice. In these cases, we used the higher resolution spectra for subsequent analyses.

In summary, the Magellan, X-Shooter and archival spectra comprise a dataset of 96 of the original 106 sample DLAs, towards 89 quasars. We also include in the sample three additional DLAs that were discovered in the course of our observations, bringing our total DLA sample to 99. See § 2.3 for details of the newly discovered DLAs. Details of the ‘missing’ 10 DLAs are reported in Table 2. We stress that these ‘missing’ DLAs, as previously mentioned, were missed only because of bad weather during our July 2009 observing run – note, that they all have  $RA \approx 13$  – and not because of some selection bias against faint quasar magnitudes or other such property. Therefore, while not ideal, their absence from our final sample should not induce any additional bias.

The MagE data were reduced using an IDL reduction package kindly provided by George Becker<sup>1</sup>. High-resolution spectra from VLT/UVES were reduced using the ESO Common Pipeline Language suite following standard recipes. The extracted spectra from all echelle orders of all exposures were combined using UVES\_POPLER<sup>2</sup>. Keck/HIRES spectra were reduced using the XIDL<sup>3</sup> reduction package. X-Shooter data were reduced with the ESO X-Shooter pipeline release 1.2.2. Continuum fitting of the reduced quasar spectrum was done using the XIDL command `x_continuum`, which allows for an interactive spline fit through data points. Because of the difficulty of determining the true continuum blue-ward of the Lyman alpha emission peak – in the Lyman alpha forest –

<sup>1</sup> Pipeline available at:

[ftp://ftp.ociw.edu/pub/gdb/mage\\_reduce/mage\\_reduce.tar.gz](ftp://ftp.ociw.edu/pub/gdb/mage_reduce/mage_reduce.tar.gz)

<sup>2</sup> UVES\_POPLER is maintained by MTM at [http://astronomy.swin.edu.au/~mmurphy/UVES\\_popler](http://astronomy.swin.edu.au/~mmurphy/UVES_popler)

<sup>3</sup> <http://www.ucoick.org/~xavier/HIRedux/index.html>

**Table 1.** DLA Sample.

Quasar	$z_{em}$	$z_{abs}$	$\log N(\text{H I})$ [ $\text{cm}^{-2}$ ]	$\Delta v$ [ $\text{km s}^{-1}$ ]	$W_{1526}$ [Å]	$W_{1548}$ [Å]	[M/H]	$f_M^a$	[Fe/H]	$f_{Fe}^b$	$l^c$	Exp. Time [s]
J0011+1446	4.9672	3.4522	21.40 $^{+0.20}_{-0.20}$	425	NA $^d$	NA $^d$	-1.12 ± 0.20	1	-1.70 ± 0.11	4	1	1800
J0011+1446	4.9672	3.6175	20.70 $^{+0.20}_{-0.20}$	145	NA $^d$	0.95 ± 0.01	-2.47 ± 0.18	14	-2.77 ± 0.08	6	1	1800
J0013+1358	3.5755	3.2812	21.50 $^{+0.10}_{-0.10}$	65	0.26 ± 0.03	0.43 ± 0.02	-1.81 ± 0.17	1	-2.14 ± 0.23	25	1	3000
J0035-0918	2.4195	2.3401	20.50 $^{+0.10}_{-0.10}$	25	0.06 ± 0.25	0.05 ± 0.25	-2.61 ± 0.12	1	-2.37 ± 0.09	1	1	4800
J0035-0918	2.4195	2.3401	20.50 $^{+0.10}_{-0.10}$	22	0.04 ± 0.01	0.02 ± 0.01	-2.72 ± 0.10	1	-2.84 ± 0.07	1	4	4800
J0124+0044	3.8292	3.0777	20.30 $^{+0.10}_{-0.10}$	142	0.11 ± 0.01	0.21 ± 0.01	-1.59 ± 0.27	13	-1.05 ± 0.10	11	3	19200 <sup>1,2,3</sup>
J0127+1405	2.4903	2.4416	20.35 $^{+0.10}_{-0.10}$	465	1.13 ± 0.02	0.77 ± 0.02	-0.70 ± 0.15	13	-1.37 ± 0.04	1	1	1700
J0139-0824	3.0162	2.6773	20.70 $^{+0.15}_{-0.15}$	108	0.61 ± 0.01	0.35 ± 0.01	-1.23 ± 0.20	1	-1.07 ± 0.05	4	3	4800 <sup>4</sup>
J0211+1241	2.9531	2.5947	20.60 $^{+0.10}_{-0.10}$	485	1.06 ± 0.03	2.24 ± 0.03	-0.58 ± 0.12	1	-0.47 ± 0.02	4	1	1800
J0234-0751	2.5276	2.3181	20.85 $^{+0.10}_{-0.10}$	45	0.13 ± 0.01	0.15 ± 0.03	-2.46 ± 0.10	1	-2.56 ± 0.04	1	1	6000
J0239-0038	3.0751	3.0185	20.35 $^{+0.10}_{-0.10}$	185	0.62 ± 0.02	1.17 ± 0.02	-0.46 ± 0.13	1	-0.51 ± 0.07	4	1	1800
J0255+0048	3.9889	3.2540	20.70 $^{+0.10}_{-0.10}$	205	1.08 ± 0.02	0.91 ± 0.02	-0.53 ± 0.10	1	-0.84 ± 0.06	4	1	3000
J0255+0048	3.9889	3.9146	21.30 $^{+0.10}_{-0.10}$	45	0.26 ± 0.01	3.14 ± 0.02	-1.70 ± 0.10	4	-1.78 ± 0.07	4	1	3000
J0338-0005	3.0500	2.2297	21.10 $^{+0.10}_{-0.10}$	165	1.32 ± 0.44	0.52 ± 0.44	-1.34 ± 0.13	1	-1.21 ± 0.11	1	1	3600
J0338-0005	3.0500	2.2297	21.10 $^{+0.10}_{-0.10}$	227	1.12 ± 0.01	0.49 ± 0.01	-1.22 ± 0.11	1	-1.74 ± 0.10	11	3	11800 <sup>4,5</sup>
J0912+0547	3.2406	3.1236	20.30 $^{+0.10}_{-0.10}$	45	NA $^d$	0.05 ± 0.02	-1.53 ± 0.17	14	-1.83 ± 0.06	1	1	1500
J0927+0746	2.5396	2.3104	20.80 $^{+0.10}_{-0.10}$	225	0.49 ± 0.01	0.55 ± 0.01	-1.12 ± 0.12	1	-2.13 ± 0.03	1	1	6300
J0942+0422	3.2755	2.3067	20.30 $^{+0.20}_{-0.20}$	138	0.32 ± 0.01	0.48 ± 0.01	-0.80 ± 0.20	1	-0.98 ± 0.02	4	4	7200
J0949+1115	3.8237	2.7584	20.95 $^{+0.10}_{-0.10}$	25	NA $^d$	1.40 ± 0.01	-1.18 ± 0.12	1	-1.14 ± 0.07	1	1	2700
J0954+0915	3.3795	2.4420	21.15 $^{+0.10}_{-0.10}$	165	1.27 ± 0.01	NA $^d$	-1.16 ± 0.11	1	-1.49 ± 0.10	1	1	2400
J1004+0018	3.0448	2.6855	21.25 $^{+0.10}_{-0.10}$	65	0.21 ± 0.01	0.30 ± 0.02	-1.59 ± 0.12	1	-1.73 ± 0.06	4	1	2400
J1004+0018	3.0448	2.5400	21.10 $^{+0.10}_{-0.10}$	125	0.58 ± 0.01	0.40 ± 0.02	-1.12 ± 0.11	1	-1.23 ± 0.03	4	1	2400
J1004+1202	2.8550	2.7997	20.95 $^{+0.10}_{-0.10}$	305	1.55 ± 0.01	1.60 ± 0.01	-0.25 ± 0.10	2	-0.76 ± 0.02	1	1	8100
J1019+0825	3.0104	2.3158	20.30 $^{+0.10}_{-0.10}$	45	0.09 ± 0.01	0.44 ± 0.01	-2.21 ± 0.11	1	-2.53 ± 0.03	1	1	1500
J1020+0922	3.6433	2.5931	21.45 $^{+0.10}_{-0.10}$	45	NA $^d$	NA $^d$	-1.71 ± 0.11	1	-1.48 ± 0.06	1	1	3400
J1022+0443	3.0811	2.7416	20.60 $^{+0.10}_{-0.10}$	185	1.10 ± 0.02	1.63 ± 0.02	-0.83 ± 0.13	1	-0.72 ± 0.04	4	1	2600
J1023+0709	3.7947	3.3777	20.40 $^{+0.10}_{-0.10}$	125	0.14 ± 0.02	0.17 ± 0.01	-2.17 ± 0.11	1	-2.14 ± 0.13	1	1	3200
J1029+1356	3.1159	2.9938	20.70 $^{+0.10}_{-0.10}$	105	0.26 ± 0.02	0.05 ± 0.02	-1.33 ± 0.15	13	-1.38 ± 0.00	3	1	2700
J1032+0149	2.4275	2.2100	20.45 $^{+0.10}_{-0.10}$	85	0.32 ± 0.01	0.43 ± 0.02	-0.88 ± 0.13	1	-1.81 ± 0.03	1	1	6300
J1037+0910	3.5784	2.8426	21.05 $^{+0.10}_{-0.10}$	125	0.36 ± 0.01	0.21 ± 0.02	-1.48 ± 0.15	13	-1.55 ± 0.12	1	1	2700
J1040-0015	4.2994	3.5450	20.75 $^{+0.10}_{-0.10}$	105	0.58 ± 0.01	0.34 ± 0.02	-1.13 ± 0.14	1	-0.85 ± 0.04	4	1	3000
J1042+0117	2.4407	2.2667	20.75 $^{+0.10}_{-0.10}$	118	0.93 ± 0.01	0.73 ± 0.01	-0.68 ± 0.10	1	-1.09 ± 0.09	1	3	4800 <sup>6</sup>
J1048+1331	3.1055	2.9196	20.65 $^{+0.10}_{-0.10}$	205	0.65 ± 0.02	0.50 ± 0.02	-0.78 ± 0.12	1	-0.80 ± 0.11	1	1	2700
J1057+0629	3.1423	2.4995	20.50 $^{+0.10}_{-0.10}$	405	1.65 ± 0.55	1.55 ± 0.55	-0.36 ± 0.11	1	-0.76 ± 0.13	1	1	2000
J1057+0629	3.1423	2.4995	20.50 $^{+0.10}_{-0.10}$	253	1.57 ± 0.01	1.49 ± 0.01	-0.41 ± 0.10	1	-0.71 ± 0.05	4	3	3600 <sup>7</sup>
J1100+1122	4.7068	4.3949	21.40 $^{+0.20}_{-0.20}$	128	0.63 ± 0.01	0.12 ± 0.01	-1.46 ± 0.16	14	-1.76 ± 0.02	4	2	5181
J1100+1122	4.7068	3.7559	20.75 $^{+0.20}_{-0.20}$	93	0.49 ± 0.01	1.63 ± 0.01	-1.42 ± 0.21	1	-0.92 ± 0.00	3	2	5181
J1106+0816	4.2670	3.2240	20.45 $^{+0.10}_{-0.10}$	85	0.22 ± 0.01	0.27 ± 0.01	-1.98 ± 0.20	14	-2.28 ± 0.13	1	1	2700
J1108+1209	3.6716	3.3963	20.65 $^{+0.10}_{-0.10}$	45	0.09 ± 0.01	0.19 ± 0.01	-2.29 ± 0.10	1	-2.69 ± 0.05	1	3	4200 <sup>6</sup>
J1108+1209	3.6716	3.5454	20.75 $^{+0.10}_{-0.10}$	128	0.75 ± 0.01	0.35 ± 0.01	-1.05 ± 0.11	1	-1.40 ± 0.02	4	3	4200 <sup>6</sup>
J1111+0714	2.8906	2.6820	20.60 $^{+0.10}_{-0.10}$	65	0.23 ± 0.01	1.18 ± 0.01	-1.32 ± 0.15	13	-2.06 ± 0.06	1	1	2400
J1111+1332	2.4195	2.2710	20.50 $^{+0.10}_{-0.10}$	25	0.07 ± 0.01	0.10 ± 0.01	-2.49 ± 0.10	1	-3.01 ± 0.03	1	1	1800
J1111+1332	2.4195	2.3822	20.45 $^{+0.10}_{-0.10}$	25	0.29 ± 0.01	0.33 ± 0.01	-1.27 ± 0.15	13	-1.81 ± 0.02	1	1	1800
J1111+1336	3.4816	3.2004	21.15 $^{+0.10}_{-0.10}$	153	0.69 ± 0.01	0.06 ± 0.01	-2.18 ± 0.15	13	-1.50 ± 0.07	1	3	3600 <sup>6</sup>
J1111+1442	3.0916	2.5996	21.35 $^{+0.15}_{-0.15}$	190	0.71 ± 0.01	0.11 ± 0.01	-1.19 ± 0.16	14	-1.49 ± 0.03	4	3	4500 <sup>7</sup>
J1133+0224	3.9899	3.9155	20.55 $^{+0.10}_{-0.10}$	25	0.15 ± 0.01	NA $^d$	-1.66 ± 0.17	14	-1.97 ± 0.07	1	1	2700
J1133+1305	3.6589	2.5975	20.55 $^{+0.10}_{-0.10}$	40	0.52 ± 0.01	0.22 ± 0.01	-1.17 ± 0.15	13	-1.94 ± 0.09	1	1	1200
J1140+0546	3.0197	2.8847	20.35 $^{+0.10}_{-0.10}$	125	0.27 ± 0.02	0.63 ± 0.02	-0.95 ± 0.15	13	-0.50 ± 0.04	4	1	2400
J1142-0012	2.4858	2.2578	20.40 $^{+0.10}_{-0.10}$	25	0.31 ± 0.01	0.20 ± 0.01	-0.85 ± 0.17	13	-1.64 ± 0.02	1	1	4200
J1151+0552	3.2406	2.9287	20.85 $^{+0.10}_{-0.10}$	165	1.32 ± 0.01	0.70 ± 0.02	-1.03 ± 0.12	1	-1.05 ± 0.07	1	1	3000
J1153+1011	4.1272	3.7950	21.35 $^{+0.10}_{-0.10}$	25	0.26 ± 0.02	0.45 ± 0.02	-2.07 ± 0.15	13	-2.08 ± 0.02	2	1	2700
J1153+1011	4.1272	3.4695	20.75 $^{+0.10}_{-0.10}$	65	0.30 ± 0.01	0.92 ± 0.02	-0.96 ± 0.14	1	-1.52 ± 0.00	3	1	2700
J1155+0530	3.4752	3.3261	21.05 $^{+0.10}_{-0.10}$	213	1.17 ± 0.01	0.28 ± 0.01	-0.65 ± 0.10	1	-1.32 ± 0.03	1	3	18600 <sup>9,6</sup>
J1155+0530	3.4752	2.6077	20.50 $^{+0.10}_{-0.10}$	27	0.11 ± 0.01	0.14 ± 0.01	-1.76 ± 0.14	1	-2.10 ± 0.01	1	3	18600 <sup>9,6</sup>
J1201+0116	3.2330	2.6852	21.00 $^{+0.15}_{-0.15}$	91	0.41 ± 0.01	0.38 ± 0.01	-1.77 ± 0.16	14	-2.07 ± 0.01	1	4	4775
J1208+0043	2.7213	2.6084	20.45 $^{+0.10}_{-0.10}$	205	0.24 ± 0.01	0.28 ± 0.01	-1.92 ± 0.10	1	-1.04 ± 0.12	4	1	2700
J1211+0422	2.5416	2.3766	20.65 $^{+0.10}_{-0.10}$	114	0.29 ± 0.01	0.90 ± 0.01	-1.19 ± 0.11	1	-1.58 ± 0.05	4	4	9000
J1211+0902	3.2905	2.5835	21.30 $^{+0.10}_{-0.10}$	328	1.62 ± 0.01	1.78 ± 0.01	-0.84 ± 0.10	1	-1.09 ± 0.01	4	3	27365 <sup>10,11,7</sup>
J1220+0921	4.1103	3.3090	20.40 $^{+0.20}_{-0.20}$	125	0.07 ± 0.01	1.65 ± 0.01	-2.48 ± 0.22	1	-1.89 ± 0.00	3	1	3000
J1223+1034	2.7613	2.7194	20.45 $^{+0.10}_{-0.10}$	345	0.45 ± 0.02	2.85 ± 0.02	-1.14 ± 0.15	13	-1.88 ± 0.07	1	1	2100
J1226+0325	2.9769	2.5078	20.95 $^{+0.10}_{-0.10}$	445	1.03 ± 0.02	1.11 ± 0.02	-0.96 ± 0.11	1	-1.78 ± 0.04	1	1	2400
J1226-0054	2.6169	2.2903	20.70 $^{+0.10}_{-0.10}$	305	1.84 ± 0.01	1.23 ± 0.02	-0.88 ± 0.13	1	-0.83 ± 0.05	4	1	3000
J1228-0104	2.6553	2.2625	20.40 $^{+0.10}_{-0.10}$	98	0.64 ± 0.43	0.52 ± 0.53	-0.92 ± 0.12	1	-1.41 ± 0.01	1	3	3600 <sup>7</sup>

<sup>a</sup> Flag describing the metallicity measurement: (1) Si measurement; (2) Zn measurement; (4) = S measurement; (13) mix of limits; (14) Fe measurement + 0.3; (15) Fe Limit + 0.3<sup>b</sup> Flag describing the Fe Measurement: (1) Fe abundance; (2) Fe lower limit; (3) Fe upper limit; (4) Ni abundance offset by -0.1; (5) Cr abundance offset by -0.2; (6) Al abundance; (11) Fe limits from a pair of transitions; (13) Limit from Fe+Ni<sup>c</sup> Instrument Used: 1 = MagE (FWHM~71 km s<sup>-1</sup>), 2 = XShooter (FWHM~59 km s<sup>-1</sup>), 3 = UVES (FWHM~8 km s<sup>-1</sup>), 4 = HIRES (FWHM~8 km s<sup>-1</sup>)<sup>d</sup> NA indicates either no spectral coverage or severe blending that precluded an equivalent width measurement**Table Notes.** –VLT Program ID Number: 1: 069.A-0613; 2: 071.A-0114; 3: 073.A-0653; 4: 074.A-0201; 5: 080.A-0014; 6: 080.A-0482; 7: 081.A-0334; 8: 080.A-0482; 9: 076.A-0376; 10: 067.A-0146; 11: 073.B-0787; 12: 067.A-0078; 13: 068.A-0600; 14: 072.A-0346; 15: 079.A-0404

Table 1 – continued DLA Sample.

Quasar	$z_{em}$	$z_{abs}$	$\log N(\text{HI})$ [ $\text{cm}^{-2}$ ]	$\Delta v$ [ $\text{km s}^{-1}$ ]	$W_{1526}$ [ $\text{\AA}$ ]	$W_{1548}$ [ $\text{\AA}$ ]	[M/H]	$f_M^a$	[Fe/H]	$f_{Fe}^b$	$I^c$	Exp. Time [s]
J1228-0104	2.6553	2.2625	$20.40^{+0.10}_{-0.10}$	125	$0.44 \pm 0.01$	$0.24 \pm 0.01$	$-0.90 \pm 0.16$	13	$-0.57 \pm 0.08$	4	1	2400
J1233+1100	2.8857	2.8206	$20.35^{+0.10}_{-0.10}$	185	$0.69 \pm 0.03$	$0.49 \pm 0.03$	$-0.54 \pm 0.23$	13	$-1.52 \pm 0.05$	1	1	3000
J1233+1100	2.8857	2.7924	$20.60^{+0.10}_{-0.10}$	365	$1.02 \pm 0.03$	$0.90 \pm 0.03$	$-0.48 \pm 0.11$	1	$-0.69 \pm 0.14$	1	1	3000
J1240+1455	3.0847	3.0242	$20.30^{+0.10}_{-0.10}$	117	$0.37 \pm 0.01$	$0.44 \pm 0.01$	$-1.52 \pm 0.10$	1	$-1.49 \pm 0.02$	1	3	26881 <sup>5</sup>
J1246+1113	3.1541	3.0971	$20.45^{+0.10}_{-0.10}$	165	$1.00 \pm 0.02$	$1.08 \pm 0.02$	$-0.53 \pm 0.14$	1	$-0.55 \pm 0.04$	4	1	1200
J1253+1147	3.2851	2.9443	$20.40^{+0.10}_{-0.10}$	75	$0.44 \pm 0.01$	$0.29 \pm 0.01$	$-0.79 \pm 0.11$	1	$-1.12 \pm 0.09$	4	3	3600 <sup>7</sup>
J1253+1306	3.6244	2.9812	$20.60^{+0.10}_{-0.10}$	65	$0.48 \pm 0.01$	$0.18 \pm 0.01$	$-1.07 \pm 0.18$	13	$-1.14 \pm 0.11$	4	1	2700
J1257-0111	4.1117	4.0209	$20.35^{+0.10}_{-0.10}$	225	$0.58 \pm 0.01$	$0.87 \pm 0.01$	$-0.88 \pm 0.10$	4	$-1.54 \pm 0.05$	1	1	2100
J1304+1202	2.9805	2.9133	$20.55^{+0.10}_{-0.10}$	125	$0.30 \pm 0.02$	$0.82 \pm 0.02$	$-1.15 \pm 0.11$	4	$-1.89 \pm 0.06$	1	1	1200
J1304+1202	2.9805	2.9288	$20.35^{+0.10}_{-0.10}$	45	$0.16 \pm 0.02$	$0.18 \pm 0.01$	$-1.96 \pm 0.11$	1	$-2.28 \pm 0.09$	1	1	1200
J1306-0135	2.9422	2.7730	$20.60^{+0.20}_{-0.20}$	165	$0.77 \pm 0.08$	$0.35 \pm 0.08$	$-0.69 \pm 0.18$	13	$-0.07 \pm 0.10$	11	1	1000
J1309+0254	2.9392	2.2450	$20.70^{+0.10}_{-0.10}$	192	$0.89 \pm 0.02$	$0.45 \pm 0.03$	$-0.24 \pm 0.15$	13	$-0.89 \pm 0.10$	11	2	2400
J1317+0100	2.6984	2.5365	$21.55^{+0.15}_{-0.15}$	12	$0.37 \pm 0.01$	$0.42 \pm 0.02$	$-1.58 \pm 0.15$	2	$-1.87 \pm 0.02$	4	2	2400
J1330+0340	2.8219	2.3215	$21.40^{+0.10}_{-0.10}$	97	$0.55 \pm 0.02$	$0.50 \pm 0.04$	$-1.13 \pm 0.15$	2	$-1.45 \pm 0.06$	5	2	1200
J1337-0246	3.0633	2.6871	$20.60^{+0.10}_{-0.10}$	6	NA <sup>d</sup>	$0.06 \pm 0.02$	$-2.80 \pm 0.13$	1	$-2.74 \pm 0.10$	1	2	2400
J1339+0548	2.9797	2.5851	$20.60^{+0.10}_{-0.10}$	175	$0.70 \pm 0.01$	$0.95 \pm 0.01$	$-0.91 \pm 0.11$	1	$-0.99 \pm 0.03$	4	3	3600 <sup>7</sup>
J1340+1106	2.9140	2.7958	$20.85^{+0.10}_{-0.10}$	40	$0.22 \pm 0.01$	$0.09 \pm 0.01$	$-1.70 \pm 0.10$	4	$-2.02 \pm 0.01$	1	3	10800 <sup>12</sup>
J1344-0323	3.2644	3.1900	$20.95^{+0.10}_{-0.10}$	285	$1.28 \pm 0.03$	$0.38 \pm 0.03$	$-0.61 \pm 0.19$	15	$-0.91 \pm 0.10$	11	1	2200
J1353-0310	2.9745	2.5600	$20.55^{+0.10}_{-0.10}$	220	$0.96 \pm 0.01$	$0.79 \pm 0.01$	$-0.89 \pm 0.12$	1	$-1.31 \pm 0.02$	1	3	5400 <sup>7</sup>
J1358+0349	2.8888	2.8516	$20.40^{+0.10}_{-0.10}$	5	$0.04 \pm 0.01$	$0.10 \pm 0.01$	$-2.72 \pm 0.12$	1	$-2.63 \pm 0.10$	11	2	2400
J1402+0117	2.9469	2.4295	$20.30^{+0.10}_{-0.10}$	64	$0.20 \pm 0.01$	$0.22 \pm 0.01$	$-0.89 \pm 0.15$	1	$-0.85 \pm 0.12$	4	2	2400
J1450-0117	3.4663	3.1901	$21.20^{+0.10}_{-0.10}$	65	$0.92 \pm 0.03$	$1.04 \pm 0.03$	$-0.76 \pm 0.15$	13	$-1.23 \pm 0.05$	4	1	3000
J1453+0023	2.5301	2.4440	$20.35^{+0.10}_{-0.10}$	65	$0.14 \pm 0.02$	$0.24 \pm 0.02$	$-1.95 \pm 0.11$	1	$-2.46 \pm 0.05$	1	1	3600
J1550+0537	3.1318	2.4159	$20.65^{+0.10}_{-0.10}$	85	$0.13 \pm 0.01$	$0.73 \pm 0.02$	$-2.41 \pm 0.11$	1	$-2.43 \pm 0.05$	1	1	3000
J2036-0553	2.5426	2.2804	$21.20^{+0.15}_{-0.15}$	71	$0.31 \pm 0.01$	$0.09 \pm 0.01$	$-1.72 \pm 0.16$	1	$-1.71 \pm 0.10$	1	4	10800
J2049-0554	3.1981	2.6828	$20.30^{+0.10}_{-0.10}$	105	$0.09 \pm 0.01$	$0.02 \pm 0.01$	$-2.24 \pm 0.11$	1	$-2.54 \pm 0.13$	1	1	4500
J2122-0014	4.0721	3.2064	$20.30^{+0.10}_{-0.10}$	125	$0.57 \pm 0.02$	$0.63 \pm 0.02$	$-0.70 \pm 0.17$	13	$-1.53 \pm 0.04$	1	1	3000
J2141+1119	2.5091	2.4263	$20.30^{+0.10}_{-0.10}$	85	$0.12 \pm 0.01$	$0.23 \pm 0.01$	$-1.17 \pm 0.20$	13	$-1.97 \pm 0.04$	1	1	8100
J2154+1102	3.1947	2.4831	$20.70^{+0.20}_{-0.20}$	205	$0.96 \pm 0.04$	$0.93 \pm 0.04$	$-0.90 \pm 0.15$	13	$-1.03 \pm 0.10$	11	1	2700
J2222-0946	2.9263	2.3544	$20.65^{+0.10}_{-0.10}$	179	$1.23 \pm 0.01$	$1.51 \pm 0.01$	$-0.56 \pm 0.10$	4	$-0.91 \pm 0.06$	1	4	3600
J2222-0946	2.9263	2.3542	$20.65^{+0.10}_{-0.10}$	245	$1.21 \pm 0.01$	$1.47 \pm 0.01$	$-0.51 \pm 0.10$	1	$-0.64 \pm 0.02$	1	1	3600
J2238+0016	3.4674	3.3654	$20.55^{+0.10}_{-0.10}$	25	$0.12 \pm 0.01$	$0.02 \pm 0.01$	$-2.39 \pm 0.10$	1	$-1.26 \pm 0.10$	4	1	3600
J2238-0921	3.2594	2.8691	$20.65^{+0.10}_{-0.10}$	105	$0.53 \pm 0.01$	$0.27 \pm 0.01$	$-1.30 \pm 0.17$	1	$-1.14 \pm 0.06$	4	1	2400
J2241+1225	2.6307	2.4175	$21.10^{+0.10}_{-0.10}$	25	$0.39 \pm 0.01$	$0.16 \pm 0.01$	$-1.54 \pm 0.13$	1	$-2.22 \pm 0.04$	1	1	3600
J2241+1352	4.4480	4.2833	$21.05^{+0.10}_{-0.10}$	65	$0.49 \pm 0.02$	$0.22 \pm 0.02$	$-1.27 \pm 0.18$	14	$-1.57 \pm 0.09$	4	1	2700
J2315+1456	3.3492	3.2730	$20.30^{+0.10}_{-0.10}$	85	$0.24 \pm 0.01$	$0.57 \pm 0.02$	$-1.76 \pm 0.11$	1	$-2.05 \pm 0.03$	6	1	1800
J2334-0908	3.3169	3.0572	$20.40^{+0.10}_{-0.10}$	212	$0.54 \pm 0.01$	$0.57 \pm 0.01$	$-0.98 \pm 0.10$	1	$-1.50 \pm 0.00$	1	3	42720 <sup>13,11</sup>
J2343+1410	2.9130	2.6768	$20.50^{+0.15}_{-0.15}$	38	$0.20 \pm 0.01$	$0.17 \pm 0.01$	$-1.98 \pm 0.17$	14	$-2.28 \pm 0.05$	6	4	3600
J2348-1041	3.1724	2.9979	$20.55^{+0.15}_{-0.15}$	195	NA <sup>d</sup>	NA <sup>d</sup>	$-1.80 \pm 0.15$	1	$-1.40 \pm 0.14$	4	4	1800
J2350-0052	3.0254	2.6147	$21.25^{+0.10}_{-0.10}$	93	$0.38 \pm 0.01$	$0.12 \pm 0.01$	$-1.92 \pm 0.10$	1	$-2.12 \pm 0.02$	4	3	85500 <sup>14,15</sup>
J2350-0052	3.0254	2.4269	$20.45^{+0.10}_{-0.10}$	271	$1.39 \pm 0.01$	$1.06 \pm 0.01$	$-0.62 \pm 0.10$	1	$-1.08 \pm 0.00$	1	3	85500 <sup>14,15</sup>

<sup>a</sup> Flag describing the metallicity measurement: (1) Si measurement; (2) Zn measurement; (4) = S measurement, (13) mix of limits; (14) Fe measurement + 0.3; (15) Fe Limit + 0.3

<sup>b</sup> Flag describing the Fe Measurement: (1) Fe abundance; (2) Fe lower limit; (3) Fe upper limit; (4) Ni abundance offset by -0.1; (5) Cr abundance offset by -0.2; (6) Al abundance; (11) Fe limits from a pair of transitions; (13) Limit from Fe+Ni

<sup>c</sup> Instrument Used: 1 = MagE (FWHM~71 km s<sup>-1</sup>), 2 = XShooter (FWHM~59 km s<sup>-1</sup>), 3 = UVES (FWHM~8 km s<sup>-1</sup>), 4 = HIRES (FWHM~8 km s<sup>-1</sup>)

<sup>d</sup> NA indicates either no spectral coverage or severe blending that precluded an equivalent width measurement

**Table Notes.** –VLT Program ID Number: 1: 069.A-0613; 2: 071.A-0114; 3: 073.A-0653; 4: 074.A-0201; 5: 080.A-0014; 6: 080.A-0482; 7: 081.A-0334; 8: 080.A-0482; 9: 076.A-0376; 10: 067.A-0146; 11: 073.B-0787; 12: 067.A-0078; 13: 068.A-0600; 14: 072.A-0346; 15: 079.A-0404

we discuss the implications of continuum fit errors in detail in Paper II (Jorgenson et al. 2013) and note that for the metal transitions analyzed here, this is not such a problem. The atomic data of the transitions discussed in this paper (e.g. laboratory wavelengths, oscillator strengths etc.) were taken primarily from Morton 2003 (Table 2) and the meteoritic solar abundances in Table 1 of Asplund et al. (2009). All spectra used in this study are available for download at <http://www.dlaabsorbers.info>.

### 2.3 New DLA and Super Lyman Limit System (SLLS) Discoveries

In the course of this survey we discovered three new DLAs, and three new SLLS, bringing our total DLA sample to 109 DLAs, of which 99 have spectra. While we incorporate the new DLAs into the survey, the SLLSs were not included in any further analysis. Details for these new discoveries are as follows:

- J0011+1446 contains a newly discovered DLA at  $z_{abs} = 3.4522$  with  $\log N_{\text{HI}} = 21.4 \text{ cm}^{-2}$  not reported in the SDSS DR5

DLA sample (Prochaska et al. 2005) or SDSS DR7 DLA sample (Noterdaeme et al. 2009). The original target in this line of sight is a metal-poor DLA ( $[\text{M}/\text{H}] = -2.5$ ) at  $z_{abs} = 3.6175$ .

- J1019+0825 contains a SLLS at  $z_{abs} = 2.9653$  with  $\log N_{\text{HI}} = 20.15 \text{ cm}^{-2}$  and a SLLS at  $z_{abs} = 2.4373$  with  $\log N_{\text{HI}} = 19.80 \text{ cm}^{-2}$ .

- J1111+1332 contains a DLA at  $z_{abs} = 2.271$  with  $\log N_{\text{HI}} = 20.50 \text{ cm}^{-2}$  and a relatively low metallicity of  $[\text{M}/\text{H}] = -2.49$  that was not reported in the DR5 sample, but was included in the DR7 sample. Noterdaeme et al. (2009) report this DLA at  $z_{abs} = 2.273$ , with  $\log N_{\text{HI}} = 20.55 \text{ cm}^{-2}$ . This line of sight also contains the previously detected SDSS DR5 DLA at  $z_{abs} = 2.3822$  (which is not included in the DR7 sample).

- J1220+0921 contains a newly discovered proximate DLA with  $\log N_{\text{HI}} = 20.80 \text{ cm}^{-2}$  at  $z_{abs} = 4.1223$  not reported in DR5 or DR7. Because this system is likely associated with the quasar ( $z_{em} = 4.11027$ ) we do not include it in our sample analysis.

- J1233+1100 contains a newly discovered DLA at  $z_{abs} = 2.8206$  with  $\log N_{\text{HI}} = 20.35 \text{ cm}^{-2}$  and  $[\text{M}/\text{H}] = -1.29$  not reported

**Table 2.** Missing Target DLAs.

Quasar	$z_{abs}$	$\log N(\text{HI})$ [ $\text{cm}^{-2}$ ]	$z_{em}$	$i$ -band Magnitude
J1301+1246	3.0251	20.95	4.103590	18.774
J1305+0521	3.6415	20.30	4.086680	18.702
J1305+0521	3.6790	21.10	4.086680	18.702
J1325+1255	3.5497	20.40	4.140640	18.842
J1341-0303	2.7556	20.40	3.222270	18.962
J1341+0141	3.6330	20.65	4.670000	18.899
J1347+0213	3.2070	20.50	3.325270	18.985
J1353-0250	2.3624	20.30	2.411540	18.596
J1402+0146	3.2773	20.95	4.160920	18.263
J1452+0154	3.2529	21.45	3.908270	18.685

in DR5 or DR7. The original DR5 DLA in this line of sight is at  $z_{abs} = 2.7924$ .

• J1246+1113 contains a SLLS at  $z_{abs} = 2.6368$  with  $\log N_{\text{HI}} = 20.20 \text{ cm}^{-2}$  and  $[\text{M}/\text{H}] = -1.32$ , not included in the survey because its  $N_{\text{HI}}$  falls just below the DLA cut. This system was reported in the DR7 sample at  $z_{abs} = 2.636$  with  $\log N_{\text{HI}} = 20.19 \text{ cm}^{-2}$ . The original DR5 target DLA at  $z_{abs} = 3.0981$  is included in the sample (however, was not included in DR7 sample).

### 3 COLUMN DENSITY AND METALLICITY MEASUREMENTS

In this section we describe the measurement of the neutral hydrogen column density,  $N(\text{HI})$ , the column densities of various metal species expected to dominate the total metal column densities in DLAs, and the metallicity,  $[\text{M}/\text{H}]^4$ . We also conduct several tests to explore the effect of limited spectral resolution on our metallicity measurements.

#### 3.1 $N(\text{H I})$ and $[\text{M}/\text{H}]$ Measurements

We used the `x_fitdla` routine contained within the XIDL package to measure the neutral hydrogen column density,  $N_{\text{HI}}$ , for each DLA. This routine allows the user to interactively and simultaneously fit both a Voigt profile to the DLA and the surrounding continuum centered on the chosen redshift, with the goal of fitting both the core and the wings of the profile. Redshifts were determined by the centroid of the strongest, unsaturated, low-ion metal component, or in other words, the low-ion velocity component with the largest optical depth without being saturated. As pointed out by Rafelski et al. (2012), this ‘not completely quantitative’ fitting-by-eye method is justified because the errors are dominated by systematic errors attributed to continuum fitting and line-blending. Following the standard practice, such as that used by Prochaska et al. (2005) and Prochaska & Wolfe (2009), we place conservative error estimates on  $N_{\text{HI}}$  of a minimum of 0.1 dex. Figure 2 presents a comparison of the original SDSS determined  $\log N_{\text{HI}}$  values and the Magellan sample, i.e. MagE or higher resolution spectra, determined  $\log N_{\text{HI}}$ . The least squares best-fit slope through the data, indicated by the black dashed line, has slope = 1.009, not very different from slope = 1, the solid red line.

<sup>4</sup> We use the standard shorthand notation for metallicity relative to solar,  $[\text{M}/\text{H}] = \log(\text{M}/\text{H}) - \log(\text{M}/\text{H})_{\odot}$

We used the standard apparent optical depth method (AODM; Savage & Sembach (1991)) to derive the column density of every available metal species in each DLA. Metallicities were typically determined from the Si II  $\lambda 1808$  line if available. In Table 1 columns 8 and 9, we report the derived metallicity and a descriptive flag, respectively, for each object.

When deriving metallicities from medium-resolution (FWHM  $\sim 70 \text{ km s}^{-1}$ ) spectra, one possible pitfall can lead to an underestimation of the metallicity due to the potential saturation of unresolved components. In § 3.2, we describe the efforts we have made to ameliorate these effects.

In Figure 3 we plot the metallicities of the entire sample versus the DLA absorption redshift. Different symbols/colors indicate the ion used to determine  $[\text{M}/\text{H}]$ . Targets for which high-resolution spectra were available are indicated by larger chartreuse circles. It is immediately seen by eye that there is not a strong apparent evolution with redshift. We provide a detailed discussion of potential redshift evolution and comparison with other DLA surveys in § 4.

#### 3.2 The Influence of Medium-Resolution Spectra in Determining $[\text{M}/\text{H}]$ : Applying Flux-based Saturation Corrections

The potential saturation of unresolved spectral features has long been a known issue confronting spectral observations of absorption lines. In the context of DLAs and the determination of DLA gas metallicity, this issue was first discussed by Prochaska et al. (2003b), and later by Penprase et al. (2010), who demonstrated that measuring metallicities from medium-resolution spectra, particularly in the high equivalent width regime, can lead to an underestimation of the true metallicity because of a failure to account for unresolved and potentially saturated spectral components. Prochaska et al. (2003b) found that in a comparison of Keck ESI ( $R \sim 7,000$ ) and Keck HIRES ( $R \sim 50,000$ ) spectra, the observed differences in the derived column densities were significant when the equivalent width was  $> 1 \text{ \AA}$ . Penprase et al. (2010), who conducted a survey for metal-poor DLAs, analyzed simulations of a single OI  $\lambda 1302$  line and concluded that in the equivalent width range of  $W = 0.050 \text{ \AA} - 0.130 \text{ \AA}$ , a saturation correction should be applied, whereas at  $W > 0.130 \text{ \AA}$ , the line must be considered saturated.

Given the MagE resolution of FWHM  $\sim 71 \text{ km s}^{-1}$  ( $R \sim 4100$ ), we have attempted to account for the possibility of unresolved saturation in our determination of metallicities from the MagE spectra. In the following sections we report on several tests we performed in order to determine the best possible corrections, if any, to make.

##### 3.2.1 Corrections Test 1: Simulated Data

We note that saturation determined purely from an equivalent width measurement can be misleading in the case of wide, complex velocity profile systems. Rather, we define, as done by Herbert-Fort et al. (2006), a normalized flux level below which an absorption line is considered saturated. Herbert-Fort et al. (2006) found that normalized intensities  $F_{min}/F_q < 0.4$ , where  $F_{min}$  is the minimum absorbed flux and  $F_q$  is the unabsorbed quasar flux, are typically saturated in Keck/ESI data.

To determine this level for the Magellan/MagE spectra we simulated spectra to match the typical observed MagE spectra, i.e. resolution  $\sim 71 \text{ km s}^{-1}$  and  $S/N \sim 30$ . We analyzed single velocity

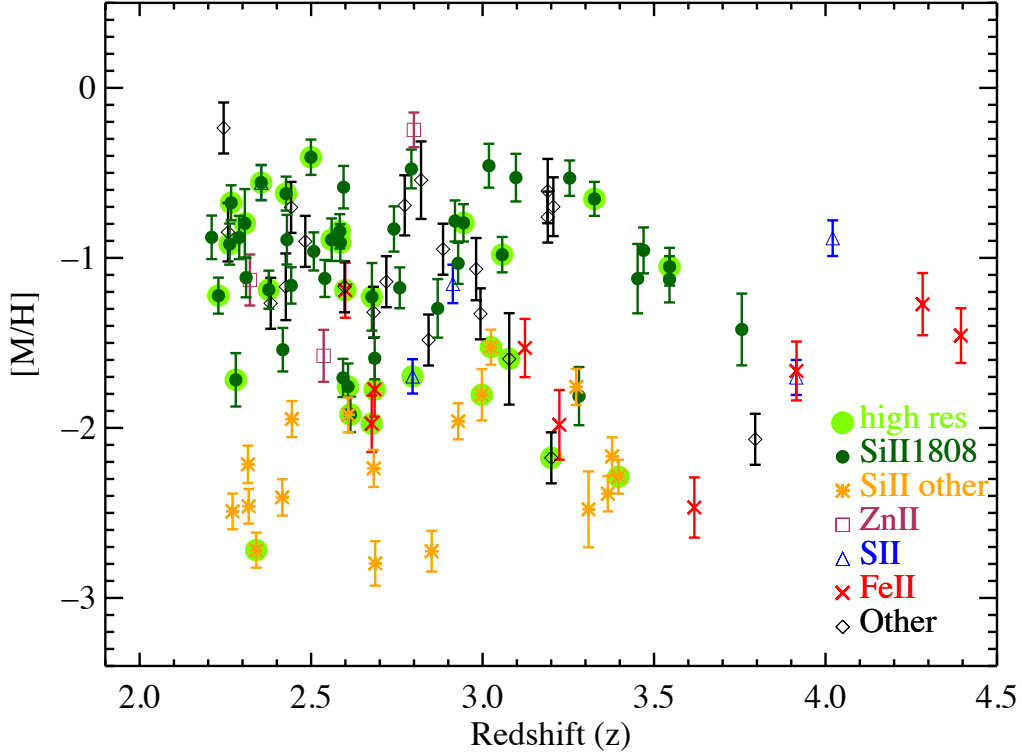


**Figure 3.**  $[M/H]$  versus redshift for the Magellan DLA sample with the ion used to determine metallicity indicated. These metallicity measurements have been made after applying the saturation criterion of  $F_{min}/F_q < 0.65$  but include no additional corrections based on flux. High-resolution data (either HIRES or UVES) are indicated by the larger chartreuse circle and have no corrections for saturation. The black diamonds indicated by ‘Other’ are determined by a combination of limits, while orange circles labeled ‘SiII other’ are determined by either Si II  $\lambda 1304$ , Si II  $\lambda 1526$  or an average of the two.

component absorption lines of OI  $\lambda 1302$ , SiII  $\lambda 1304$ , SiII  $\lambda 1526$ , and SiII  $\lambda 1808$  with a range of column density values and Doppler parameters, to determine the flux level above which the AODM returned a column density value,  $N_{AODM}$ , similar to the true (i.e. input) value,  $N_{true}$ . The results of these simulations are shown in Figure 4, where we plot  $\Delta N$ , the difference in  $N_{true}$  and  $N_{AODM}$ , versus the minimum flux of the absorption line, for three different Doppler parameters,  $b = 10, 7.5$  and  $5 \text{ km s}^{-1}$ . While there is a large variation depending on the line and column density/Doppler parameter chosen, we note that for  $b = 10 \text{ km s}^{-1}$ , any absorption line with a normalized flux of greater than  $F_{min}/F_q > 0.65$  was prone to deviations from  $N_{true}$  of 0.5 dex or less. We take  $b = 10 \text{ km s}^{-1}$  to be a representative Doppler parameter because, while it might be slightly larger than a typical individual velocity component, most low-ion profiles contain blends of several velocity components qualitatively similar to larger Doppler parameter profiles. Therefore, we have implemented an automatic saturation criterion that flags any line where  $F_{min}/F_q < 0.65$  as saturated and not to be used to determine  $[M/H]$ .

In addition, we used the results of the simulations to attempt to apply flux-based saturation corrections to the lines used to determine  $[M/H]$  in the MagE spectra. Shown as the red solid lines in Figure 4 is the best-fit polynomial curve to the data for  $b = 10, 7.5$  and  $5 \text{ km s}^{-1}$  (from left to right). We then applied this fit to make corrections to the derived column density of the ion used

to determine  $[M/H]$  based upon the minimum flux within the profile. It is apparent from Figure 4 that as the Doppler parameter becomes smaller, the necessary column density corrections can become rather significant. While we take note that this is an issue to be aware of, using the justification stated above, we apply the corrections based on the best-fit line for Doppler parameter  $b = 10 \text{ km s}^{-1}$ . In Figure 5 we show the resulting changes to the metallicity versus redshift after applying this flux-based correction for  $b = 10 \text{ km s}^{-1}$  to the MagE and X-Shooter data. We note that applying these flux-based metallicity corrections does not make a large change in the final result – the mean correction of the lines that required a correction is only 0.18 dex. Therefore, given the uncertainties and variations in Doppler parameters, along with the fact that this exercise indicates these will not make a large difference, we decided not to apply this flux based correction to the sample.

### 3.2.2 Corrections Test 2: Smoothed high-resolution Data

In reality, the low-ion velocity structure of DLAs usually consists of many velocity components with various degrees of blending, rather than a simple, single velocity component. In light of this fact, we performed a similar analysis as above, however, this time instead of using simulated data at MagE resolution, we used high-resolution data from our sample and smoothed it to the resolution of the MagE spectra, adding noise such that the SNR of the smoothed spectrum



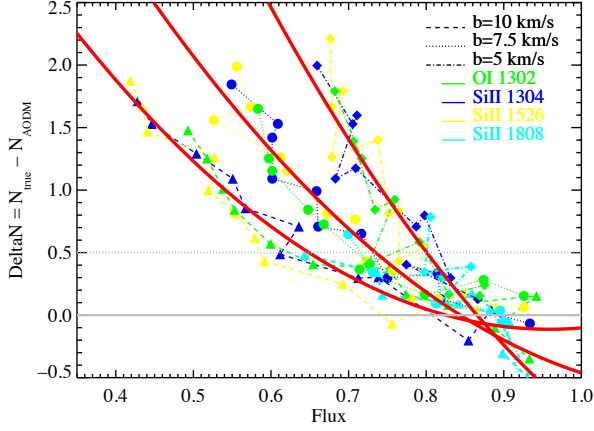


**Figure 4.** Results of simulations to estimate the effects of medium-resolution MagE spectra on metallicity determination. Using simulated spectra that match those of the MagE data we inserted and measured lines of OI and SiII with a range of column densities and Doppler  $b$  parameters. The above figure plots  $\Delta N$ , the difference between the true/input column density ( $N_{true}$ ) and the output column density ( $N_{AODM}$ ) measured by the AODM technique versus the minimum flux of the absorption line. The different colors represent the different ion transitions used and the symbols and line styles connecting the points indicates the Doppler parameter assumed. Overplotted as a solid red line is a best-fit polynomial curve to the data for  $b = 10, 7.5$  and  $5 \text{ km s}^{-1}$ , from left to right. This fit can be used to make corrections to the derived column density of the ion used to determine  $[M/H]$  based upon the minimum flux within the profile.

matched that of our typical MagE spectra,  $\text{SNR} \sim 20 \text{ pixel}^{-1}$ . We choose the eight high-resolution spectra that contained coverage of the large range of Fe II transitions from  $\lambda 1608\text{\AA} - \lambda 2600\text{\AA}$ . In this way we were able to 1) have a good measure of the true  $N(\text{Fe II})$ ,  $N_{true}$ , from the unsaturated high-resolution Fe II transitions, and 2) explore the effects of measuring  $N_{AODM}$  from a wide range of oscillator strength transitions in the context of realistic velocity profiles smoothed to the resolution of MagE. Figure 6 contains example Fe II velocity profiles for two of these DLAs, DLA 1155+0530 and DLA 0338–0005. The left column is the original high resolution UVES spectrum, while the right column is the same spectrum smoothed to the MagE resolution with noise added such that  $\text{SNR} \sim 20 \text{ pixel}^{-1}$ . In Figure 7 we show that, perhaps surprisingly, the effect of underestimation of the true column density may not be so severe in reality.

In Figure 7 we plot  $\Delta N$  versus  $F_{min}/F_q$  for eight DLAs, where  $\Delta N = N_{true} - N_{AODM}$ .  $N_{true}$  is measured from the non-saturated Fe II transitions in the high-resolution data, while  $N_{AODM}$  is measured for each of the Fe II transitions in the smoothed spectrum. Note that the transitions of large unabsorbed flux (right side of plot) are associated with weak transitions for which upper limits on  $N_{AODM}$  were returned, making the resultant  $\Delta N$  negative. The large black circle denotes the Fe II transitions belonging to DLA 1155+0530, a somewhat unusual case, as it contains a single relatively narrow absorption feature (see Figure 6, where the velocity width of 90% of the optical depth,  $\Delta v_{90} = 27 \text{ km s}^{-1}$ ) and therefore probes a specific range in flux. However, it is seen from these lines that even in this case of a narrow absorption feature, the MagE-resolution AODM does not greatly underestimate the column density.

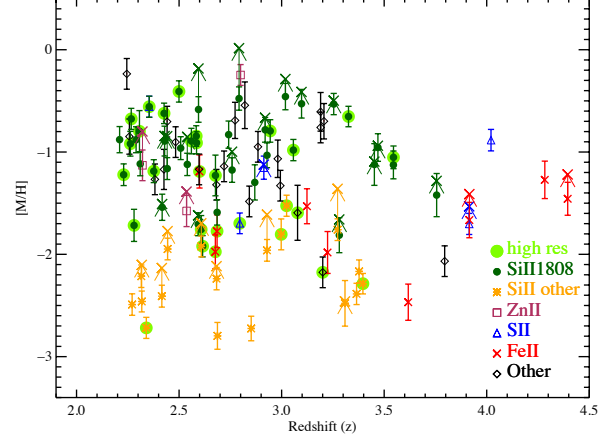


**Figure 5.**  $[M/H]$  versus redshift for the Magellan DLA sample with the ion used to determine metallicity indicated. Flux corrections assuming  $b = 10 \text{ km s}^{-1}$  have been applied. The ‘X’ indicates the new flux-corrected metallicity and the arrow connects the original to new point.

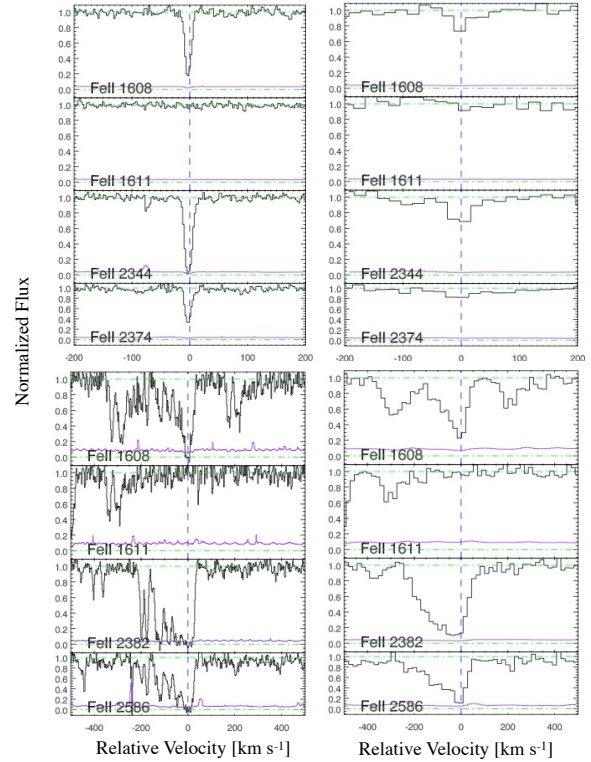


**Figure 6.** Example Fe II velocity profiles used to create Figure 7. The top two panels show a selection of Fe II velocity profiles from DLA 1155+0530. On the left is the original UVES spectrum ( $\text{FWHM} \sim 8 \text{ km s}^{-1}$ ) and on the right is the same spectrum smoothed to MagE resolution ( $\text{FWHM} \sim 70 \text{ km s}^{-1}$ ) at a  $\text{SNR} = 20$ . The bottom two panels show a selection of Fe II velocity profiles for DLA 0338–0005, with the original UVES spectrum on the left and the smoothed spectrum on the right.



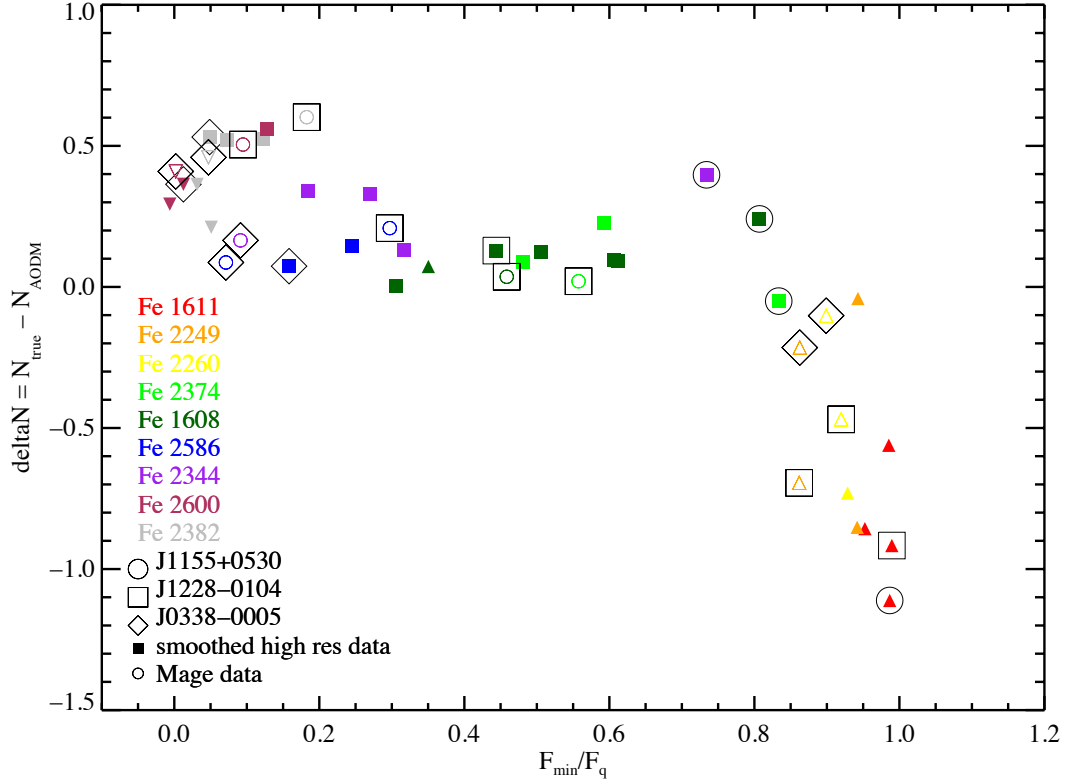


**Figure 7.** The results of Corrections Test 2 plotted as  $\Delta N$  versus  $F_{min}/F_q$ . Colors indicate different Fe II lines in rainbow order of increasing oscillator strength. Triangles indicate that the AODM measurement was an upper limit (upward pointing) or lower limit (downward pointing). Open circles represent data from DLAs that also had MagE spectra (so these measurements are based on the MagE spectrum). Filled squares are the data derived from the smoothed spectrum. Larger open symbols denote the particular object, i.e. dark green square and dark green circle located at  $F_{min}/F_q \sim 0.45$  are both inside a larger black square, indicating they are the Fe II  $\lambda 1608$  line from the smoothed UVES J1228–0104 spectrum and the original MagE J1228–0104 spectrum respectively.

**Table 3.** MagE versus high resolution.

DLA	feature	MagE	high res.	$\Delta_{MagE-highres}$
DLA 0035–0918 <sup>a</sup>	[M/H]	$-2.61 \pm 0.12$	$-2.72 \pm 0.10$	0.11
	$\Delta v_{90}$ (km s <sup>-1</sup> )	25	22	3
DLA 0338–0005 <sup>b</sup>	$W_{1526}$ (Å)	$0.06 \pm 0.25$	$0.04 \pm 0.05$	0.02
	[M/H]	$-1.34 \pm 0.13$	$-1.22 \pm 0.11$	0.12
DLA 1057–0629 <sup>b</sup>	$\Delta v_{90}$ (km s <sup>-1</sup> )	165	227	-62
	$W_{1526}$ (Å)	$1.32 \pm 0.44$	$1.12 \pm 0.14$	0.20
DLA 1228–0104 <sup>b</sup>	[M/H]	$-0.36 \pm 0.11$	$-0.41 \pm 0.10$	0.05
	$\Delta v_{90}$ (km s <sup>-1</sup> )	405	253	152
DLA 2222–0946 <sup>a</sup>	$W_{1526}$ (Å)	$1.65 \pm 0.55$	$1.57 \pm 0.18$	0.08
	[M/H]	$> -0.90$	$-0.92 \pm 0.12$	0.02
DLA 0338–0005 <sup>b</sup>	$\Delta v_{90}$ (km s <sup>-1</sup> )	125	98	27
	$W_{1526}$ (Å)	$0.64 \pm 0.43$	$0.44 \pm 0.13$	0.20
DLA 1057–0629 <sup>b</sup>	[M/H]	$-0.52 \pm 0.10$	$-0.56 \pm 0.10$	0.04
	$\Delta v_{90}$ (km s <sup>-1</sup> )	245	179	66
DLA 2222–0946 <sup>a</sup>	$W_{1526}$ (Å)	$1.23 \pm 0.47$	$1.22 \pm 0.01$	0.01

<sup>a</sup> Keck/HIRES data

<sup>b</sup> VLT/UVES data

From this analysis we conclude that over a range of oscillator strengths, for a range of real, low-ion velocity profiles, the underestimation caused by application of the AODM technique to medium-resolution data is generally less than  $\sim 0.5$  dex, and for some oscillator strength/flux/column density combinations is less than 0.3 dex. Interestingly, even in the range of flux  $F_{min}/F_q \sim 0.4$ –0.6 the

underestimation is not large. These results give us confidence that our choice of minimum flux  $F_{min}/F_q < 0.65$  as the definition of a saturated transition is a conservative limit that will ensure we are making a minimum amount of metallicity underestimation due to the application of AODM on medium-resolution data.

### 3.2.3 Corrections Test 3: Direct Comparison of MagE and High-resolution Data

As an additional check on the robustness of the MagE metallicities, we compared the results for the five sample DLAs observed with both MagE and a high-resolution spectrograph. We summarize the results in Table 3 and make note of the fact that, by chance, these five DLAs happen to span a large range in metallicity,  $\Delta v_{90}$  and equivalent width of the Si II  $\lambda 1526$  ( $W_{\lambda 1526}$ ) transition. In Figure 8 we plot the velocity profile of the low-ion used to estimate the metallicity, as well as another transition for reference, for each DLA in Table 3. It is reassuring to see from this comparison that the derived [M/H] agree quite well – with a maximum difference of 0.12 dex.

We note that for three DLAs, DLA 0338–0005, DLA 1057–0629 and DLA 2222–0946, there is a relatively large discrepancy in the  $\Delta v_{90}$  measurement of the MagE versus high resolution spectrum. As described in § 5.1, the way in which  $\Delta v_{90}$

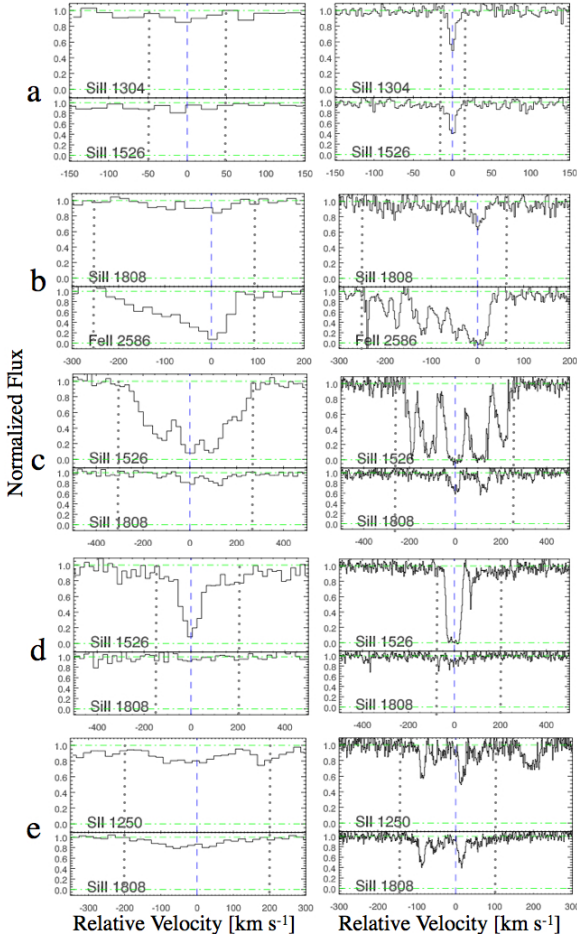


**Figure 8.** Low-ion velocity profiles used to estimate the metallicity,  $[M/H]$ , in each DLA in Table 3. The panels, labelled a–e represent DLAs 0035–0918, 0338–0005, 1057–0629, 1228–0104 and 2222–0946, respectively. Each panel shows the MagE spectrum on the left and the high resolution spectrum on the right. In all panels, the transition used to estimate the metallicity is shown, as well as another transition for reference. The grey dotted lines denote the velocity range over which the metallicity was calculated. In panels b, c, and d the Si II  $\lambda 1808$  line was used to determine the metallicity, while in panel a, both Si II  $\lambda 1304$  and Si II  $\lambda 1526$  were used, and in panel e, Si II  $\lambda 1808$  was used in the case of the MagE spectrum, while Si II  $\lambda 1250$  was used for the high resolution spectrum.

is measured, by moving pixel-by-pixel across the velocity profile, means that it is dependent upon the resolution of the spectrum, and, as a result, lower resolution spectra tend to overestimate the true  $\Delta v_{90}$ . While we have attempted to correct for this effect, as discussed in § 5.1, it is clear that perhaps, in the case of these 3 DLAs, the correction is not enough. In addition, we point out that in these cases, the velocity interval over which the  $\Delta v_{90}$  is calculated is different for the different resolution spectra, as seen in Figure 8. If we instead calculate the  $\Delta v_{90}$  in the MagE spectrum using the same velocity interval as that used for the high resolution spectrum, we find that for two DLAs, the discrepancies in  $\Delta v_{90}$  become smaller. Specifically,  $\Delta v_{90}^{MagE} = 305 \text{ km s}^{-1}$  and  $205 \text{ km s}^{-1}$  for DLA 1057–0629 and DLA 2222–0946, respectively. On the other hand, DLA 0338–0005 became slightly more discrepant when integrated over the high resolution velocity profile, with  $\Delta v_{90} = 125$

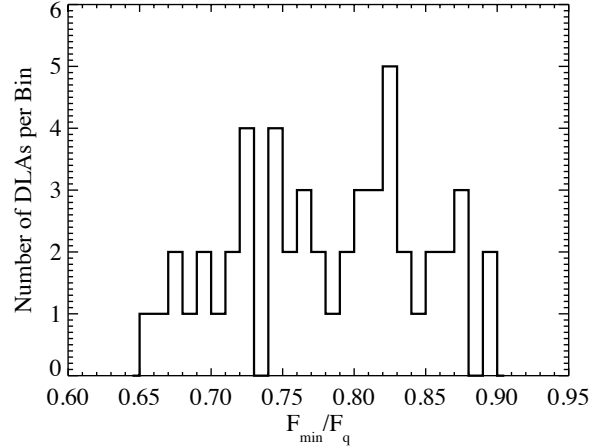


**Figure 9.** Distribution of  $F_{min}/F_q$  values of the transitions used in determining the metallicities for 51 of the MagE and X–Shooter spectra. The remaining 19 were determined from a combination of limits and are not shown here.

$\text{km s}^{-1}$ . As a result, we stress that one must use caution when interpreting the measurements of  $\Delta v_{90}$  from lower resolution spectra.

### 3.2.4 Summary of Corrections Tests and Final Adopted Metallicities

Taking the results of these three corrections tests into consideration, we conclude that with the possible exception of some rare cases, resolution-motivated corrections to the AODM derived column densities from the medium-resolution MagE data will not make a significant difference to the results, provided we apply the minimum flux requirement of  $F_{min}/F_q < 0.65$ . Therefore, we report in Table 1 the AODM-derived metallicities of the MagE and X–Shooter data without additional flux-based corrections unless otherwise noted. In Figure 9 we show the distribution of  $F_{min}/F_q$  values of the transitions used in determining the metallicities for 51 of the MagE and X–Shooter spectra. It is clear that the  $F_{min}/F_q$  values are not clustered at the set threshold (0.65) and therefore, we expect that our results do not strongly depend on the threshold value we use. An additional 19 systems, labeled in Figure 3 as ‘Other’ and determined from a combination of limits, are not shown.

## 4 COSMIC METALLICITY EVOLUTION OVER REDSHIFTS $z = 2.2 - 4.4$ ?

In this section we investigate the evidence for redshift evolution in the DLA metallicities of the Magellan sample. We compare our sample to that of Rafelski et al. (2012) who found a metallicity evolution of  $-0.22 \pm 0.03$  dex per unit redshift over the redshift range  $z = 0.09 - 5.06$ . Rafelski et al. (2012, hereafter R12) report metallicity measurements for 47 new DLAs, 30 with  $z_{abs} > 4$ , and incorporate an additional 195 DLAs from the literature. Their literature sample includes a sample created earlier by Prochaska et al. (2003a) who – for the first time detected a statistically significant evolution in the cosmic mean metallicity of  $-0.26 \pm 0.07$  dex per unit redshift. The Prochaska et al. (2003a) sample consists of 125 DLAs,  $\sim 75$  of which were drawn from the literature, while the other  $\sim 50$  were taken by them with ESI.

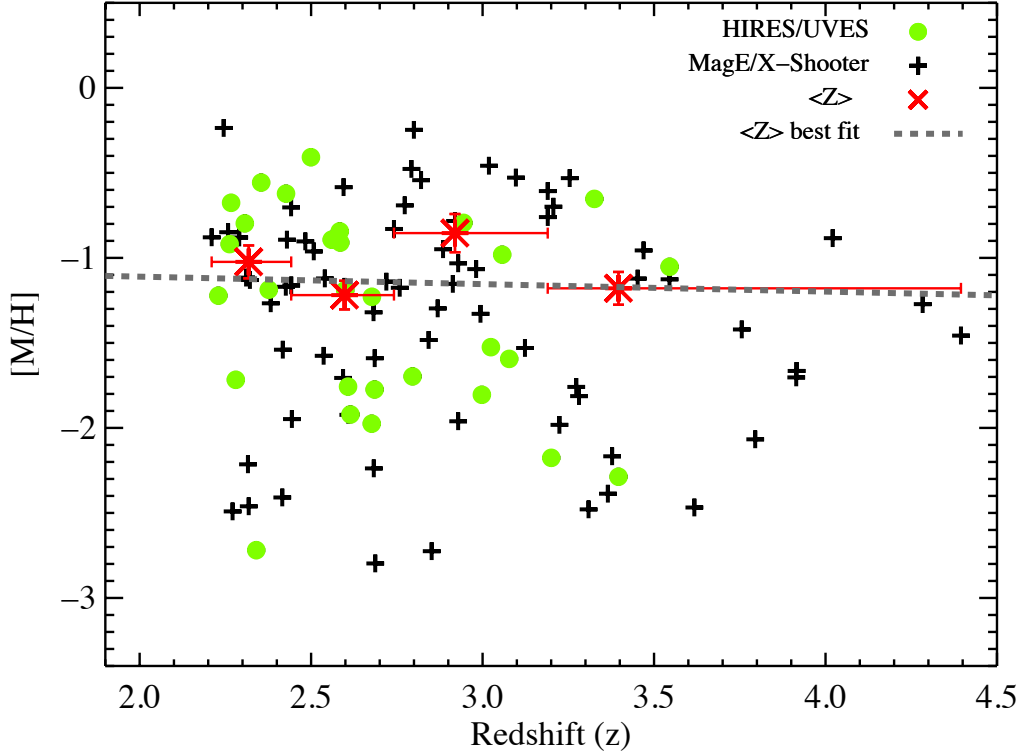


**Figure 10.**  $[M/H]$  versus redshift for the Magellan DLA sample. The sample is divided into four redshift bins containing equal numbers of DLAs. The red points denote the cosmic mean metallicity with  $1\sigma$  confidence interval bootstrap error bars as defined in the text. The grey dashed line represents the linear best-fit to the binned data points,  $\langle Z \rangle = (-0.04 \pm 0.13)z - (1.06 \pm 0.36)$ .

Following these works, we calculate the cosmological mean metallicity defined as,  $\langle Z \rangle = \log[\sum_i 10^{[M/H]_i} N(HI)_i / \sum_i N(HI)_i]$  where  $i$  represents the DLA in a given redshift bin. In order to roughly match the bin sizes of R12, we divide the Magellan sample into four redshift bins containing an equal number of DLAs (25 DLAs/bin), except for the lowest redshift bin that contains only 24 DLAs. We calculate  $\langle Z \rangle$  and plot the results in Figure 10 in red with  $1\sigma$  confidence bootstrap error bars. As explained in R12, because the  $\langle Z \rangle$  is dominated by sample variance rather than statistical error, the bootstrap method best describes a realistic uncertainty. For the sake of comparison, we have applied the same bootstrap error method as that described in R12. Overplotted as a grey dashed line is the linear least-squares fit through the  $\langle Z \rangle$  values and their uncertainties, described by  $\langle Z \rangle = (-0.04 \pm 0.13)z - (1.06 \pm 0.36)$ . Perhaps surprisingly, this slope is consistent with no redshift evolution in metallicity over the redshift range of the Magellan sample,  $z = 2.21 - 4.40$  and possibly in contrast with the results of R12, who found  $\langle Z \rangle = (-0.22 \pm 0.03)z - (0.65 \pm 0.09)$  over the range  $z = 0.09 - 5.06$ . Given the slope of the Magellan sample, in seeming contrast with the previously published surveys, we first consider in greater detail whether the difference in detected evolution between the Magellan sample presented here and the sample of R12 is significant and then discuss the possible effects of potential biases.

#### 4.1 How different are the Magellan and R12 samples?

One potential source of confusion in comparing the evolution implied by the Magellan and the R12 samples could be attributed to the difference in redshift ranges, with the Magellan sample covering  $z = 2.21 - 4.40$  and the R12 sample covering the larger range of  $z = 0.09 - 5.06$ . For example, if we constrain the R12 sample to include *only* the data within the redshift range of the Magellan sample, we obtain a best-fit result,  $\langle Z \rangle = (-0.16 \pm 0.07)z - (0.82 \pm 0.22)$ , see the top left panel of Figure 11. This ‘flattening’ of the slope of the R12 sample – from  $-0.22$  to  $-0.16$  – when excluding the DLAs in the highest and lowest redshift ranges indicates the significant contribution of these bins to the detection of evolution. If we instead restrict the redshift range to  $z = 2.2 - 3.5$ , where the majority of the Magellan sample lies, we find an identical result,  $\langle Z \rangle = (-0.16 \pm 0.12)z - (0.82 \pm 0.35)$ .

We have performed the opposite test and calculated the effect on the evolution of cosmic metallicity of combining the Magellan sample with the highest and lowest redshift bins of the R12 sample. In the top right panel of Figure 11 we plot the results of this test, which give  $\langle Z \rangle = (-0.21 \pm 0.03)z - (0.63 \pm 0.08)$ , similar to the slope determined from the R12 sample. This similarity again emphasizes the importance of the highest and lowest redshift bins in measuring metallicity evolution. Indeed, the slope obtained from *just* the highest and lowest redshift bins of the R12 sample is  $\langle Z \rangle = (-0.23 \pm 0.03)z - (0.59 \pm 0.08)$ .

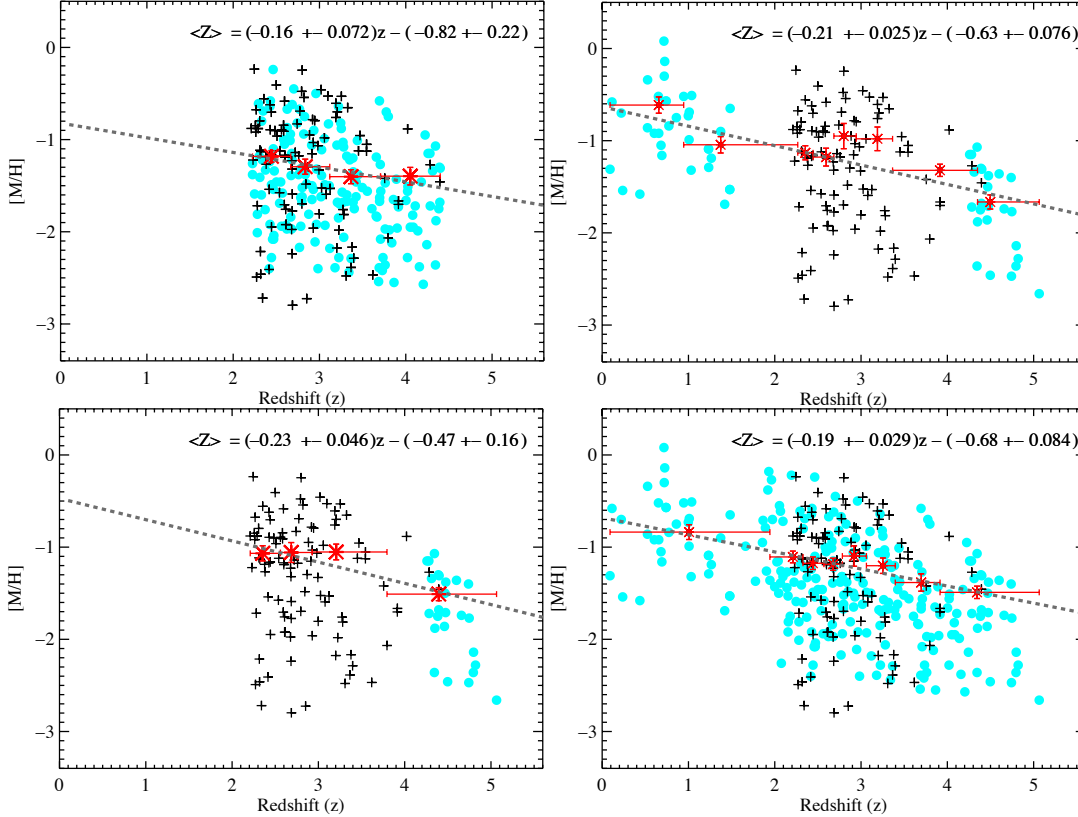


**Figure 11.**  $[M/H]$  versus redshift for the Magellan sample (black crosses) and various subsets of the R12 sample (cyan circles). Overplotted in red are the cosmological mean values in either 4 or 8 bins of equal numbers of DLAs with  $1\sigma$  error bars determined as described in the text. The dashed grey lines are linear fits to the  $\langle Z \rangle$  data points. **Top left panel:** The R12 sample taken over only the redshift range of the Magellan sample (Magellan sample points shown only for reference). It is seen that when the R12 sample is constrained to this smaller redshift range the slope is flatter ( $-0.16$ , see inset) than for the entire high- $z$  sample, indicating the importance of the highest and lowest redshift ranges in the determination of significant metallicity evolution. **Top right panel:** Magellan sample combined with only the highest and lowest redshift bins of the R12 sample. **Bottom left panel:** Magellan sample and only the highest redshift bin of the R12 sample. **Bottom right panel:** The Magellan and the R12 sample combined.

However, as R12 notes, the lowest redshift bin ( $z \sim 0 - 1.5$ ) included in the R12 sample presents a problem because the DLAs in this bin were selected based upon strong MgII absorption, typically associated with high metallicity, and therefore constitute a not-unbiased representation of the low redshift end. Given this fact, we repeat the above test, this time excluding the lowest redshift bin. In the bottom left panel of Figure 11 we plot the metallicity evolution derived from the Magellan sample – which alone has a slope of  $-0.04$  – and *only* the highest redshift bin from the R12 sample. The resulting evolution,  $\langle Z \rangle = (-0.23 \pm 0.05)z - (0.47 \pm 0.16)$ , even neglecting the lowest, metallicity-biased redshift bin, is again similar to that of the R12 sample (slope =  $-0.22$ ). This result emphasizes the importance of the highest redshift bin in determining an evolution and, assuming this bin is not biased (however, see § 4.2.2), leads us to the conclusion that a possible explanation for the apparent lack of evolution in the Magellan sample is simply an effect of the limited redshift range covered. Finally, in the bottom right panel of Figure 11 we calculate the cosmological mean metallicity evolution of both the Magellan and the R12 samples combined. While combining the samples produces the highest significance simply from including the most DLAs, we note that caution must be employed in interpreting this result, as shown above and in § 4.2, the Magellan sample is relatively unbiased with re-

spect to the R12 sample and it is likely that there are significant biases in this result.

In an attempt to minimize the effects of the redshift range differences of the samples, we performed a bootstrap analysis in which we selected DLAs from the R12 sample according to the redshift distribution of the Magellan sample, and then calculated the resulting cosmological means and best-fit slope. We repeated this process 10,000 times, always randomly selecting the R12 sample DLAs with replacement according to the redshift distribution of the Magellan sample. In Figure 12 we plot a histogram of the resultant slopes. The mean slope, plotted as a cyan vertical line, is  $-0.25$ , with a standard deviation of  $0.17$  (dotted cyan lines). We compare this with the slope of the Magellan sample,  $-0.04 \pm 0.13$ , shown as a vertical black line. It is clear that the bootstrap distribution from the R12 sample overlaps considerably with the error margin from the Magellan sample. Indeed, there is a  $\sim 10\%$  chance of obtaining a slope equal to the Magellan sample ( $-0.04$ ) or flatter if the R12 sample is selected according to the redshift distribution of the Magellan sample. In other words, after considering the differences in their redshift distributions, the lack of metallicity evolution found in the Magellan sample is not in conflict with that of the R12 sample.

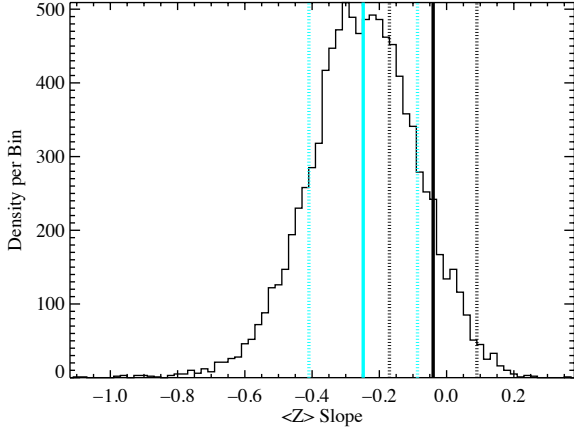


**Figure 12.** Distribution of slopes of the evolution of  $\langle Z \rangle$  derived from 10,000 bootstrap samples of the R12 metallicity distribution according to the redshift distribution of the Magellan sample. It is seen that the slope of the R12 sample (mean =  $-0.25 \pm 0.16$ , shown in cyan), when taken over the redshift range of the Magellan sample, is, considering error bars (dotted lines), strictly consistent with that of the Magellan sample, shown here in black at  $-0.04 \pm 0.13$ . Given the R12 sample with the redshift distribution of the Magellan sample, there is a  $\sim 10\%$  probability of obtaining a slope equal to or flatter than the Magellan sample.

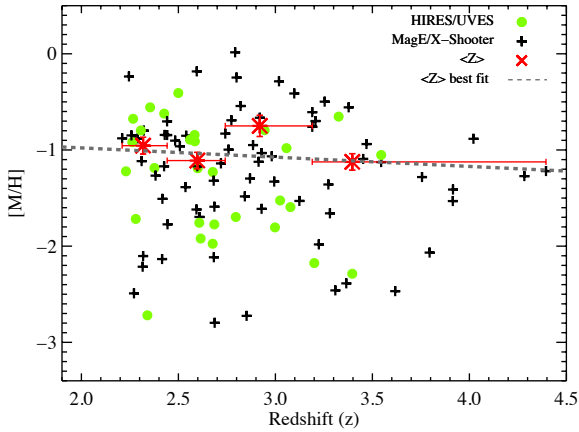


**Figure 13.**  $[M/H]$  versus redshift for the flux-corrected Magellan sample, assuming  $b = 10 \text{ km s}^{-1}$ . The sample is divided into four redshift bins containing equal numbers of DLAs. The red points denote the cosmic mean metallicity with  $1\sigma$  confidence interval bootstrap error bars as defined in the text. The grey dashed lines represent the linear best-fit to the binned data points,  $\langle Z \rangle = (-0.10 \pm 0.11)z - (0.79 \pm 0.31)$ .

## 4.2 Assessment of Potential Biases

### 4.2.1 Bias in the Magellan sample?

We first note that the detection of  $\sim$ zero evolution in the Magellan sample is not dependent on the highest redshift DLAs – in fact, if we exclude the three objects at  $z_{\text{abs}} > 4$  we derived a similar result,  $\langle Z \rangle = (-0.01 \pm 0.13)z - (1.15 \pm 0.38)$ . We do note however, that if we remove the three lowest metallicity DLAs from the Magellan sample, all with  $[M/H] < -2.7$ , we obtain  $\langle Z \rangle =$

$(-0.10 \pm 0.12)z - (0.87 \pm 0.32)$ . While this is still technically consistent with no evolution, it is interesting that the removal of just three (low metallicity) DLAs moves the slope in a direction consistent with the R12 sample. Part of this change in slope is caused by a slight change in binning due to the removal of three DLAs. Specifically, the high metallicity, high  $N_{\text{HI}}$  DLA 1344–0323, is moved from the highest redshift bin to the neighboring bin, creating some of the change in slope. However, we note that the metallicity values of the three low metallicity DLAs are relatively secure: one object, DLA 0035–0918, is taken from Keck/HIRES data (Cooke et al. 2011), while the other two, DLA 1337–0246 and DLA 1358+0349 are supported by expected/similar  $[Fe/H]$  measurements, i.e. the  $[Fe/H]$  values are similar and less than 0.3 dex different than the  $[\alpha/H]$  value as expected for low-metallicity DLAs, i.e. Figure 11 of R12. Is it by chance that the Magellan sample contains three relatively low metallicity DLAs at  $z_{\text{abs}} \sim 2.5$ ? We discuss this question further in the next section, § 4.2.2.

Although we have already shown in § 3 that by applying a minimum flux cut (here,  $F_{\text{min}}/F_q < 0.65$ ), additional flux-based column density corrections will likely not have a large effect on the overall measurements, we did investigate the effects of applying the flux-based correction on the evolution of  $\langle Z \rangle$ . In Figure 13 we plot the results of applying the flux-based column density correction shown in Figure 4 for a Doppler parameter  $b = 10 \text{ km s}^{-1}$  (these corrections are also shown in Figure 5). It is seen that this does have some effect on the slope, with a best-fit of  $\langle Z \rangle = (-0.10 \pm 0.11)z - (0.79 \pm 0.31)$ . Interestingly, the application of the flux-based corrections does move the measured evolution in  $\langle Z \rangle$  closer to the results of R12. However, while the change is insufficient for full agreement we cannot rule out that this could be a contributing effect to the detected difference in the  $\langle Z \rangle$  evolution of the Magellan and R12 samples.

### 4.2.2 Bias in the R12 Sample?

In total, the R12 sample contains 33 DLAs with medium-resolution Keck/ESI spectra only, 22 DLAs with Keck/HIRES spectroscopy, and an additional 195 DLAs taken from the literature. For their newly presented metallicities, R12 state that they did not apply any flux corrections to their medium-resolution Keck/ESI data because they followed-up all likely problematic candidates with Keck/HIRES in order to obtain a good measurement of the metallicity.

In contrast to the Magellan sample that was specifically designed *a priori* to be uniformly selected, as demonstrated by the good agreement in H I column density distribution,  $f(N_{\text{HI}})$ , between the Magellan sample and the SDSS sample (i.e. Figure 1), the R12 sample contains a large number ( $\sim 195$ ) of DLAs taken from the literature. While R12 state that care was taken to avoid including DLAs from biased samples, it is still illuminating to compare the H I column density distribution of the R12 sample with that of the SDSS to assess any potential level of bias. We show the results of this comparison in Figure 14, where a two sided Kolmogorov-Smirnov (K-S) test shows that the probability of the R12 sample and the SDSS DR5 (left) and SDSS DR7 (right) sample to be drawn from the same parent population is  $P_{KS} = 1 \times 10^{-6}$ , and  $P_{KS} = 0.05$  respectively. It is seen that there may be a slight deficit of low- $N_{\text{HI}}$  systems and overabundance at the high- $N_{\text{HI}}$  end.

Indeed, if we assume that the metallicity distribution of the R12 sample is an unbiased representation of the true DLA metallicity distribution, we should be able to compare it with that of



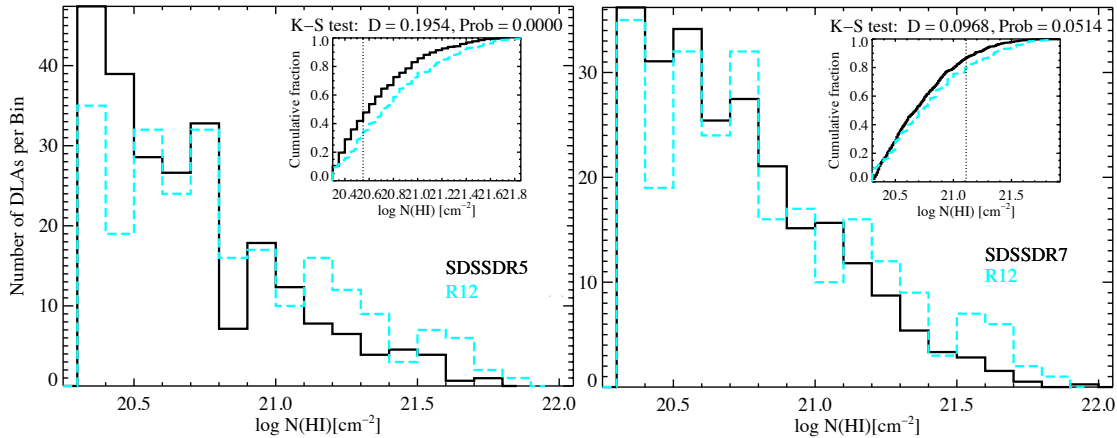


**Figure 14.**  $N_{\text{HI}}$  histogram comparing the R12 sample (cyan, dashed line) with the scaled SDSSDR5 (Prochaska et al. 2005) distribution, left, and the scaled SDSSDR7 (Noterdaeme et al. 2009) distribution, right. A K-S test indicates that the probability they are drawn from the same parent population is  $P_{K-S} = 1 \times 10^{-6}$  and  $P_{K-S} = 0.05$ , respectively.

the Magellan sample. In order to facilitate comparison between the samples we consider only those DLA within the redshift range of the Magellan sample and fit the metallicity distribution with a Gaussian, as shown in Figure 8 of R12. We derive a best-fit Gaussian with mean metallicity  $[M/H] = -1.54$  and  $\sigma=0.46$ . Assuming this distribution is correct, we would expect less than  $\sim 0.5\%$  of any sample to have  $[M/H] \leq -2.72$ . The Magellan sample contains 3/99 DLAs, or  $\sim 3\%$  of the sample with  $[M/H] \leq -2.72$ , an interesting, but perhaps not significant difference from the distribution expected from the R12 sample.

As previously mentioned, an additional potentially large bias in the R12 sample, also discussed by R12, is the inclusion of the DLAs in the lowest redshift bin ( $z \sim 0 - 1.5$ ). Because these DLAs were generally first identified by their strong MgII absorption, it would be unsurprising to find they are biased towards higher metallicities.

### 4.3 Conclusions on Metallicity Evolution

The previously detected cosmic mean metallicity evolution derived from DLAs was measured by R12, to be  $\langle Z \rangle = (-0.22 \pm 0.03)z - (0.65 \pm 0.09)$  over the range  $z = 0.09 - 5.06$ . In this paper, we present an independent, albeit smaller DLA sample that found essentially no evolution,  $\langle Z \rangle = (-0.04 \pm 0.13)z - (1.06 \pm 0.36)$  over the redshift range  $z = 2.21 - 4.40$ . We note that the majority of this sample falls between  $z = 2.21 - 3.50$ , and that the slopes of the R12 and Magellan samples are, strictly speaking, consistent with each other at the  $2\sigma$  level.

As discussed in § 4.1 much of the power of the detected evolution in the R12 sample comes from the highest and lowest redshift bins covering a redshift space not probed by the Magellan sample. While this fact and the biases outlined in § 4.2.1 and § 4.2.2 may prohibit a direct comparison of the measurements of cosmic metallicity evolution (or lack thereof), a relevant question remains: Is there evolution in metallicity over the redshift range probed by the Magellan sample,  $z \sim 2 - 4$ ?

In answering this question, we consider the following facts:

1) The Magellan sample was designed *a priori* to be uniformly selected and is more consistent with the  $N_{\text{HI}}$  frequency distribu-

tion function of the parent SDSS sample, 2) the slope found by the R12 sample is heavily weighted by the lowest and highest redshift ends, and 3) the bootstrapping of the R12 sample within the redshift range of the Magellan sample indicates that the samples are not inconsistent with each other. Given this evidence, we propose that the slope of metallicity evolution of DLAs between  $z \sim 2 - 4$  may be flatter than that found by the R12 sample and closer to the most likely value found in the Magellan sample presented here.

## 5 OTHER DLA DIAGNOSTICS

In this section we present an analysis of several additional DLA diagnostics that are important in determining DLA gas properties such as the width of the low-ion velocity profile,  $\Delta v_{90}$ , and the equivalent width of the Si II  $\lambda 1526\text{\AA}$  line,  $W_{\lambda 1526}$ .

### 5.1 $\Delta v_{90}$

The  $\Delta v_{90}$  statistic is defined to be a measure of the velocity interval that contains 90% of the integrated optical depth of the low-ion metallic gas (Prochaska & Wolfe 1997).  $\Delta v_{90}$  is typically measured from an unsaturated low-ion transition and represents the kinematic state of the bulk of the gas. In past DLA surveys several authors, i.e. Ledoux et al. (2006) and Prochaska et al. (2008), have shown this statistic to be strongly correlated with DLA metallicity. They interpret this as a sort of mass-metallicity relation and derive slopes that are similar to those found for the mass-metallicity relationships in samples of local, low-metallicity galaxies.

Following the practice of Prochaska et al. (2008), who analyze the effects of lower resolution spectra in determining the  $\Delta v_{90}$  parameter and find that for their medium-resolution Keck/ESI spectra, the  $\Delta v_{90}$  values are biased high by approximately half of the instrumental FWHM, we assume that our MagE spectra (with FWHM  $\sim 71 \text{ km s}^{-1}$ ) are biased high by  $\sim 35 \text{ km s}^{-1}$ . Therefore, we reduce the  $\Delta v_{90}$  values obtained from the MagE data by  $35 \text{ km s}^{-1}$ , in order to account for this systematic effect. Likewise, for the X-Shooter data (FWHM  $\approx 59 \text{ km s}^{-1}$ ) we reduce the  $\Delta v_{90}$



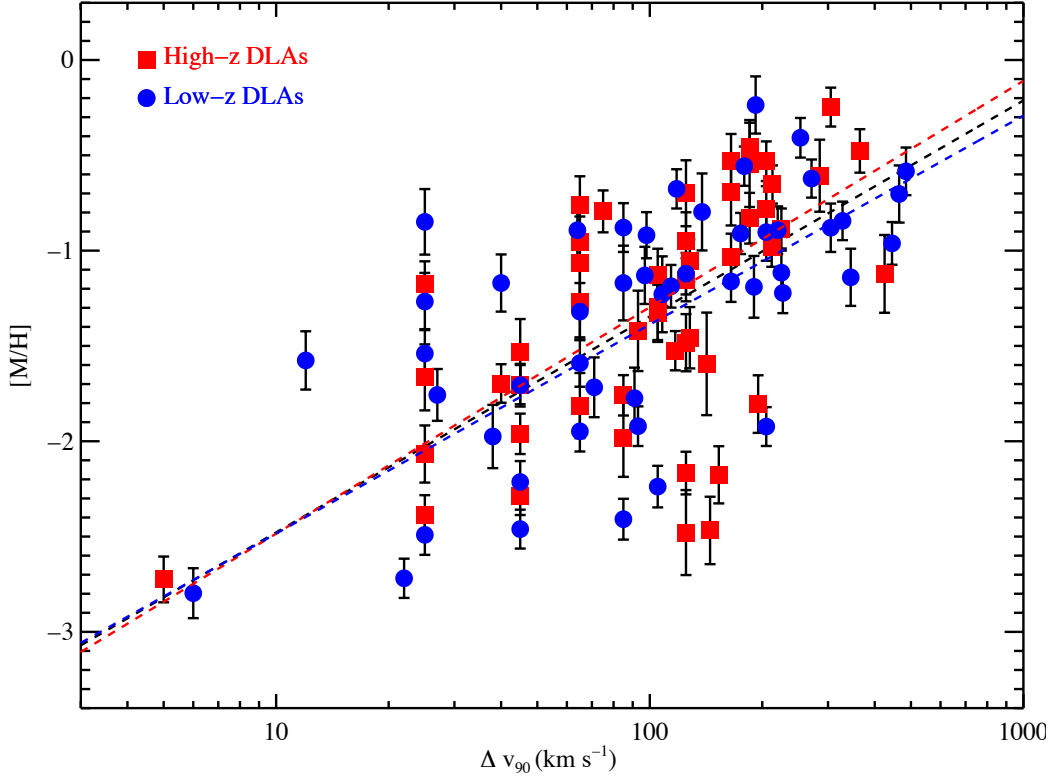


**Figure 15.** Metallicity versus  $\Delta v_{90}$ , a measure of the kinematic state of the gas, for the Magellan sample. Red squares denote the high- $z$  bin with all points greater than or equal to the median  $z_{abs} = 2.74$ , while blue circles denote the low- $z$  bin. While there does appear to be a correlation between  $\Delta v_{90}$  and  $[M/H]$ , there is no evidence for evolution with redshift, as seen by the similarity of the red and blue distributions. The dashed lines represent power law fits as described in the text for the entire sample (black), the high- $z$  sample (red) and the low- $z$  sample (blue).

values by  $30 \text{ km s}^{-1}$ . We report the  $\Delta v_{90}$  statistic in column 5 of Table 1.

In Figure 15 we plot  $[M/H]$  versus  $\Delta v_{90}$  for the Magellan sample. It can be seen by eye that there is a correlation, albeit with  $\sim 1.5$  dex scatter, between  $\Delta v_{90}$  and DLA metallicity. As stated by others (Ledoux et al. 2006; Prochaska et al. 2008), this scatter is likely due to differences in impact parameter and the inclination of the galaxy over which  $\Delta v_{90}$  is measured. Statistically, the correlation is significant – the Kendall tau rank correlation provides a probability  $P(\tau) = 9.6 \times 10^{-11}$  of being due to chance alone, corresponding to significance of correlation  $> 6.4\sigma$ . This result is in agreement with previous surveys that have found similar trends, i.e. Ledoux et al. (2006); Prochaska et al. (2008).

A power law fit to the  $\Delta v_{90}$  vs.  $[M/H]$  data in Figure 15,

$$[M/H] = a + b \log(\Delta v_{90}) \quad (1)$$

drawn as the black dashed line, gives best fit parameters  $a = -3.61 \pm 0.07$  and  $b = 1.13 \pm 0.03$ . This is a somewhat flatter slope than that found by Ledoux et al. (2006), who report,  $a = -4.33 \pm 0.23$  and  $b = 1.55 \pm 0.12$ . While we hesitate to speculate in depth on the nature of this discrepancy, we point out several differences between the Ledoux et al. (2006) sample and the Magellan sample: The Ledoux et al. (2006) sample 1) is smaller (70 objects), 2) includes 13 Super Lyman-limit Systems (SLLS), which could introduce additional confusion from ionization corrections, and 3) is known to

have an  $f(N_{\text{HI}})$  distribution different than the ‘unbiased’ SDSS distribution.

The median  $\Delta v_{90}$  of the Magellan sample is  $114 \text{ km s}^{-1}$ . This is higher than the median  $\Delta v_{90}$  found by Prochaska et al. (2008),  $80 \text{ km s}^{-1}$ , and the medians found by Ledoux et al. (2006) in their high and low redshift samples,  $69$  and  $92 \text{ km s}^{-1}$ , respectively. To investigate the possibility of redshift evolution in the  $\Delta v_{90}$  parameter, as found by Ledoux et al. (2006), we split the sample into high and low redshift bins, separated by the median  $z_{abs} = 2.74$ . We find, in contrast to the results of Ledoux et al. (2006), that there is little difference between these two populations. The median metallicity and median velocity width of the two populations are  $\langle [M/H]^{highz} \rangle = -1.18 \pm 0.49$  and  $\langle \Delta v_{90}^{highz} \rangle = 125 \pm 60 \text{ km s}^{-1}$  in the high redshift bin, and  $\langle [M/H]^{lowz} \rangle = -1.17 \pm 0.37$  and  $\langle \Delta v_{90}^{lowz} \rangle = 98 \pm 71 \text{ km s}^{-1}$ , in the low redshift bin. While the metallicity is virtually unchanged, there is a slight, yet insignificant decrease in  $\Delta v_{90}$  from high to low redshift. Strictly speaking, this is opposite to the trend found by Ledoux et al. (2006), however, given the error bars it is likely not significant. This can be seen in Figure 15 where the red squares (blue circles) indicate the high (low) redshift bin. It is seen by eye that there is very little difference in the two distributions. A two sided Kolmogorov-Smirnov (K-S) test shows that the low- and high- $z$   $\Delta v_{90}$  values are entirely consistent with being drawn from the same parent population,  $P_{KS} = 0.75$ .

Performing a linear least squares fit to the high and low red-

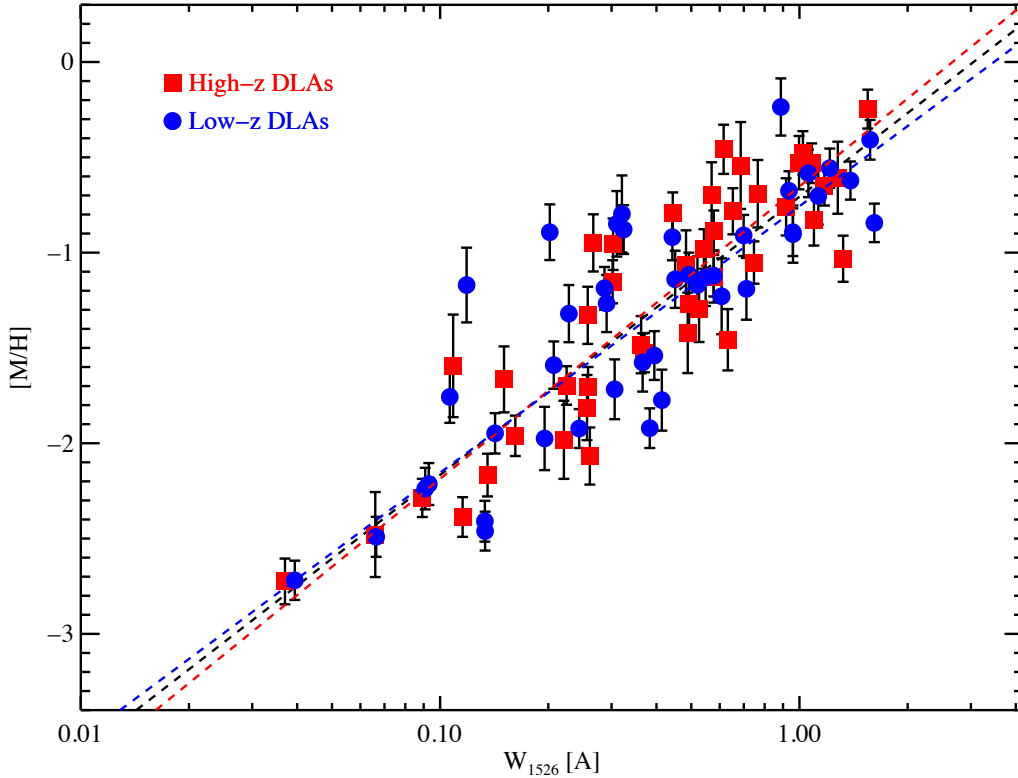


**Figure 16.** The remarkably tight correlation between Si II 1526 Å Equivalent Width versus metallicity in the Magellan sample. Red points denote the high- $z$  bin with all points greater than or equal to the median  $z_{\text{obs}} = 2.74$ , while blue points denote the low- $z$  bin. It is visually apparent that there is essentially no significant evolution with redshift. The dashed lines represent power law fits as described in the text. The average error on the  $W_{1526}$  values is  $\sim 0.013$  Å

shift samples separately gives the following best-fit parameters:  $a^{\text{high}z} = -3.67 \pm 0.10$  and  $b^{\text{high}z} = 1.19 \pm 0.05$ ;  $a^{\text{low}z} = -3.58 \pm 0.09$  and  $b^{\text{low}z} = 1.10 \pm 0.04$ . The fits are represented by the red (high- $z$ ) and blue (low- $z$ ) dashed lines in Figure 15 and show very little difference between the high and low redshift samples with the possible exception of a slight steepening of the high redshift slope.

## 5.2 $W_{\lambda 1526}$ and $W_{\lambda 1548}$

Another kinematic diagnostic often used to characterize the DLA population is the rest equivalent width, defined as  $W = W_{\text{obs}}/(1+z)$ , of various absorption lines. As explained in Prochaska et al. (2008) the  $W$  statistic is a measure of the kinematics of the system when the line used is optically thick. We report the rest equivalent widths of two transitions representing the low-ion and high-ion transitions, respectively, Si II  $\lambda 1526$  and C IV  $\lambda 1548$  in Table 1. For reference, the expected  $W_{\lambda 1526}$  of the Si II  $\lambda 1526$  line to become optically thick ( $\tau > 1$ ) is  $\approx 0.1 - 0.3$  Å, depending upon the velocity profile of the system.

We plot the results of  $W_{\lambda 1526}$  versus metallicity in Figure 16. We include only DLAs with good spectral coverage of the Si II  $\lambda 1526$  line. If there was no coverage, or if the line suffered from serious blending with an interloper or forest line, we did not include it in this analysis. Figure 16 contains a total of 86 DLAs.

Interestingly, as found by previous authors, the correlation between  $W_{\lambda 1526}$  and metallicity is significantly stronger than that be-

tween  $\Delta v_{90}$  and metallicity. The Pearson correlation coefficient is  $r = 0.76$ , as compared with  $r = 0.55$  for  $[M/H]$  with  $\Delta v_{90}$ . The results of the Kendall tau test give a probability that there is no underlying correlation and that the observed  $r$  occurs by chance alone,  $P(\tau) = 3.9 \times 10^{-19}$ , corresponding to significance of correlation  $> 9\sigma$ . Perhaps in part this is not surprising given that the equivalent width of a line should be independent of spectral resolution, as opposed to  $\Delta v_{90}$  which is clearly affected by instrumental FWHM. However, it is still surprising how tight the correlation is given that our data span the optically-thin/optically-thick transition, yet the correlation remains tight and strong everywhere. A power law fit to the data,

$$[M/H] = a + b \log(W/(1\text{Å})) \quad (2)$$

results in best-fit parameters  $a = -0.71 \pm 0.02$  and  $b = 1.46 \pm 0.03$  and is denoted by the black dashed line. While the results for the slope of the Magellan sample agree well with those of Prochaska et al. (2008) who derived best-fit parameters for their sample,  $a = -0.92 \pm 0.05$ ,  $b = 1.41 \pm 0.10$ , the y-intercepts are different by 0.05 implying that metallicities in the Magellan sample are generally higher at a given  $W$ .

As discussed in Prochaska et al. (2008), the fact that the correlation between  $[M/H]$  and  $W_{\lambda 1526}$  is even tighter than that between  $[M/H]$  and  $\Delta v_{90}$  is perhaps surprising given that the gas that determines the  $[M/H]$  – the bulk of the ISM gas measured in the low-ion components – is in general physically more related to the  $\Delta v_{90}$  statistic that is also derived from this low-ion gas. On the con-

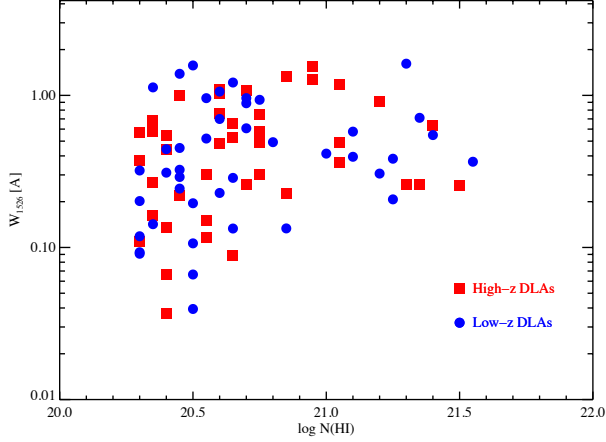


**Figure 17.**  $\log N_{\text{HI}}$  versus Si II 1526 Å Equivalent Width. The average error on the  $W_{1526}$  values is  $\sim 0.013$  Å, while the typical errors on the  $\log N_{\text{HI}}$  values are  $\pm 0.1$  dex. Red points denote the high- $z$  bin with all points greater than or equal to the median  $z_{\text{abs}} = 2.74$ , while blue points denote the low- $z$  bin.

trary, the  $W_{\lambda 1526}$  statistic can contain a large contribution from halo gas unrelated to the bulk of the galaxy. Hence, as Prochaska et al. (2008) point out, this implies a mysterious connection between the local ISM properties of the galaxy that determine  $[M/H]$  and its environment, specifically, its large scale velocity field, and has been interpreted as a mass-metallicity relation.

Taking this interpretation one step further, we propose that the large difference in scatter of the two correlations is actually evidence *supporting* the disk-like DLA scenario. Specifically, because  $W_{\lambda 1526}$  is dominated by gas at large velocities, in the outskirts or halo of the galaxy, a natural interpretation of this correlation is a mass-metallicity relation where the more massive halos are more metal enriched and contain gas at larger velocities that would contribute to the  $W_{\lambda 1526}$ . In this case, because the dark matter halo is essentially spherical, the inclination angle of the disk does not matter. On the other hand, the  $\Delta v_{90}$  parameter is more susceptible to the orientation – assuming DLAs are disk-like structures participating in some organized motion. In this case, the measured  $\Delta v_{90}$  will depend on the impact parameter and inclination angle of the disk, which would vary widely amongst DLAs and provide the source of the larger scatter in the  $\Delta v_{90} - [M/H]$  relation. Therefore, in some sense, the larger scatter in the  $\Delta v_{90} - [M/H]$  correlation along with a simultaneously smaller scatter in the  $W_{\lambda 1526} - [M/H]$  correlation is consistent with the interpretation of DLAs as disk-like structures. On the other hand, if DLAs were primarily merging clumps of gas (Haehnelt et al. 1998), it would be difficult to explain the tighter  $W_{\lambda 1526} - [M/H]$  correlation.

Dividing the  $W_{\lambda 1526}$  sample into two bins of high and low redshift reveals no evidence for any evolution in the  $W_{\lambda 1526}$  parameter with redshift. The high redshift median  $\langle W_{\lambda 1526}^{\text{high}z} \rangle = 0.49 \pm 0.23$  while the low redshift median  $\langle W_{\lambda 1526}^{\text{low}z} \rangle = 0.38 \pm 0.22$ . We note that, if  $W_{\lambda 1526}$  really is a good tracer of metallicity, then these medians imply a *decrease* in metallicity with decreasing redshift, contrary to what one would expect if DLAs are indeed tracing the build-up of metals over cosmic time. Interestingly, this is the same behavior as seen in  $\Delta v_{90}$ , where the median value of the  $\Delta v_{90}$  parameter actually decreases slightly with redshift – an opposite trend

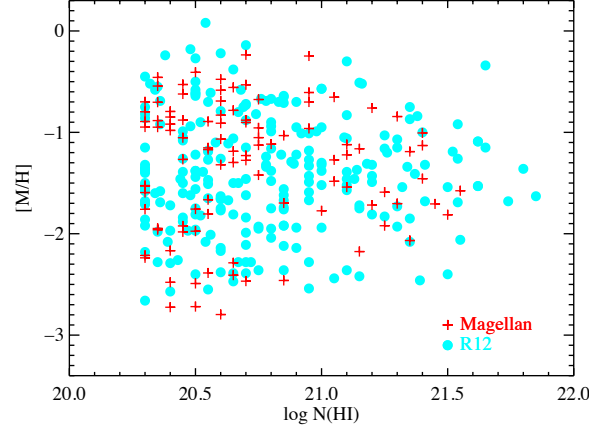


**Figure 18.**  $\log N_{\text{HI}}$  versus  $[M/H]$  for the Magellan sample (red crosses) and the R12 sample (cyan circles). It is clear that the correlation between  $\log N_{\text{HI}}$  and  $W_{1526}$  at low  $W_{1526}$  seen in Figure 17, is related to a similar trend seen here with  $[M/H]$  in the Magellan sample. However, the R12 sample (cyan circles) does not seem to show this same trend, indicating that perhaps rather than having a physical origin, it is the result of small number statistics.

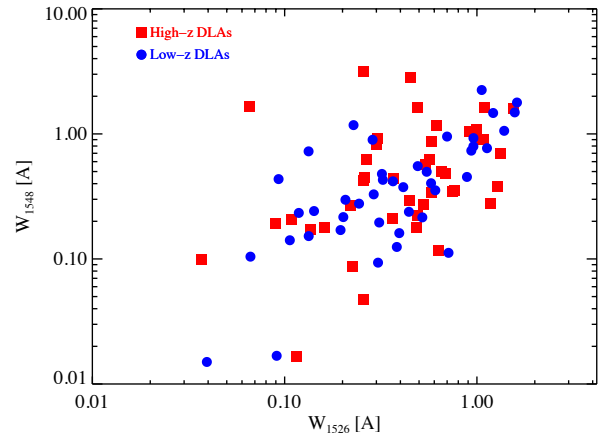


**Figure 19.** C IV 1548 Å Equivalent Width versus Si II 1526 Å Equivalent Width of the Magellan sample. Red points denote the high- $z$  bin with all points greater than or equal to the median  $z_{\text{abs}} = 2.74$ , while blue points denote the low- $z$  bin. The average error on the  $W_{1526}$  and  $W_{1548}$  values is  $\sim 0.013$  Å and  $\sim 0.015$  Å, respectively.

to that reported in  $\Delta v_{90}$  by Ledoux et al. (2006). However, we note that within the error bars, there is no significant change in the median values. Again, this can be seen in Figure 16 where we have plotted the high (low) redshift points as red squares (blue circles). The two populations virtually overlap. Best fit lines to the data produce the dashed red and blue lines for the high and low redshift bins respectively. The best-fit linear parameters are  $a^{\text{high}z} = -0.65 \pm 0.03$  and  $b^{\text{high}z} = 1.53 \pm 0.05$ ;  $a^{\text{low}z} = -0.76 \pm 0.03$  and  $b^{\text{low}z} = 1.40 \pm 0.04$ . Any difference in the low and high redshift populations is not very significant as the two sided Kolmogorov-Smirnov test gives the probability that the two are drawn from the same parent population as  $P_{KS} = 0.77$ .

We also examine  $W_{\lambda 1526}$  as a function of  $N_{\text{HI}}$ , as seen in Figure 17. Similar to Prochaska et al. (2008) (Figure 7) we see a trend for increasing  $N(\text{H I})$  with increasing  $W_{\lambda 1526}$  up to  $W_{\lambda 1526} \sim 0.2 \text{ \AA}$ , where the data then become a scatter plot. The results of the Kendall tau test give a significance of correlation  $>2.6\sigma$  ( $P(\tau) = 9.5 \times 10^{-3}$ ). One immediate question raised by Figure 17 is why there are no DLAs with low  $W_{\lambda 1526}$  ( $\sim \leq 0.2 \text{ \AA}$ ) and high  $N_{\text{HI}}$ ? Is there some physical mechanism to explain this apparent ‘forbidden zone’?

In looking at the behavior of the metallicity of the Magellan sample as a function of  $N_{\text{HI}}$  (see Figure 18, red crosses), we see a similar ‘forbidden zone’ in the region of low metallicity and high  $N_{\text{HI}}$ . That we see this same trend is not surprising, as we have shown above that  $W_{\lambda 1526}$  is tightly correlated with metallicity. However, when we compare this with the R12 sample – cyan circles in Figure 18 – we see that any type of correlation between  $N_{\text{HI}}$  and metallicity seems to disappear. Indeed, the results of the Kendall tau test,  $P(\tau) = 0.63$ , indicate no correlation, leading us to conclude that any correlation seen at low  $W_{\lambda 1526}$  is likely the result of small number statistics.

A correlation is seen for the relation between  $W_{\lambda 1526}$  and the equivalent width of high-ion gas,  $W_{\lambda 1548}$  as seen in Figure 19. The linear Pearson correlation coefficient is  $r=0.43$  and a positive correlation between the two variables is detected at the  $>5.5\sigma$  level ( $P(\tau) = 3.2 \times 10^{-8}$ ). A similar correlation was reported by Prochaska et al. (2008) and has been interpreted as a sign that the low and high-ion gas is subject to a common gravitational potential well (Wolfe & Prochaska 2000; Maller et al. 2003).

### 5.3 Mg II $\lambda 2796$ Equivalent Width versus $[\text{M}/\text{H}]$ and $N_{\text{HI}}$

We find some evidence for a correlation between metallicity and the equivalent width of the MgII  $\lambda 2796 \text{ \AA}$  line,  $W_{\lambda 2796}$ , in the Magellan sample, see Figure 20. The results of the Kendall tau test show a significance of correlation  $>2.5\sigma$  ( $P(\tau) = 1.2 \times 10^{-2}$ ). This is a similar trend to that found by Murphy et al. (2007), who report a  $4.2\sigma$  significant correlation between  $W_{\lambda 2796}$  and  $[\text{M}/\text{H}]$  in a sample of 49 DLAs and strong sub-DLAs. Murphy et al. (2007) conclude that this correlation is a result of the connection between an absorber’s metallicity and the mechanism for producing and dispersing the velocity components, since the saturated  $W_{\lambda 2796}$  is most sensitive to the kinematic spread of the gas.

A power law fit to the data, like that in equation 2, results in best-fit parameters  $a = -1.38 \pm 0.02$  and  $b = 0.97 \pm 0.06$  and is shown in Figure 20 by the black dashed line. Dividing the already small sample (27 DLAs) into high and low redshift bins about the median redshift of this sample,  $z = 2.44$ , gives best-fit parameters of the power law fits to the subsamples:  $a^{\text{high}z} = -1.47 \pm 0.04$  and  $b^{\text{high}z} = 0.93 \pm 0.12$  and  $a^{\text{low}z} = -1.25 \pm 0.04$  and  $b^{\text{low}z} = 1.10 \pm 0.08$ . These fits are shown in Figure 20 by the red and blue dashed lines, respectively. While these fits may indicate some evolution in  $W_{\lambda 2796}$  with redshift – indeed the median  $W_{\lambda 2796}$  decreases from high to low redshift,  $\langle W_{\lambda 2796}^{\text{high}z} \rangle = 1.51 \pm 0.79 \text{ \AA}$  to  $\langle W_{\lambda 2796}^{\text{low}z} \rangle = 1.23 \pm 0.62 \text{ \AA}$  – given the sizable error bars, this change may not be significant.

We find no evidence for a correlation between  $W_{\lambda 2796}$  and  $N_{\text{HI}}$  as seen in Figure 21. The results of the Kendall tau test,  $P(\tau) = 0.52$ , provide essentially no evidence for correlation. The noticeable absence of systems with *both* large  $\log N_{\text{HI}}$  and  $W_{\lambda 2796}$ , in the upper right corner of the plot, is not statistically significant because of the small number of DLAs available with  $W_{\lambda 2796}$  measurements.

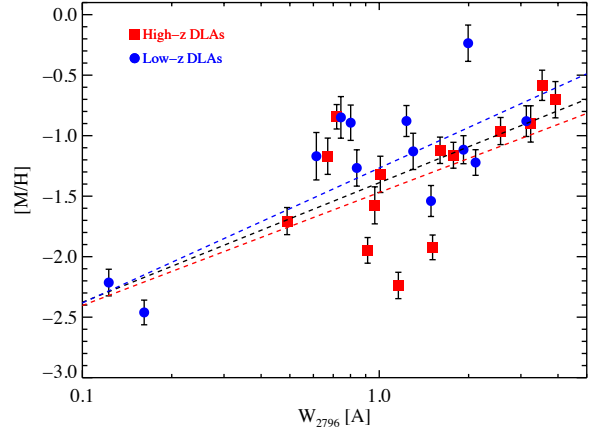


**Figure 20.**  $[\text{M}/\text{H}]$  versus MgII  $\lambda 2796 \text{ \AA}$  equivalent width ( $W_{2796}$ ) of the Magellan sample that contained spectral coverage of the MgII  $\lambda 2796 \text{ \AA}$  line. The mean error on  $W_{2796}$  is  $\sim \pm 0.12 \text{ \AA}$ . Red squares denote the high redshift points, while blue circles represent the low redshift points, where the sample was split on the median redshift,  $z_{\text{abs}}=2.44$ . While the correlation is not highly significant ( $\sim 2.5\sigma$ ), there is a trend for the highest equivalent width systems to also have high metallicities. There is also a slight trend for increased metallicities in the lower redshift sample for a given  $W_{2796}$ .

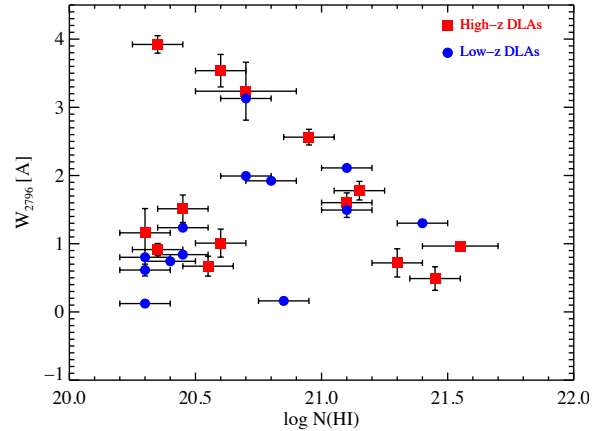


**Figure 21.** MgII  $\lambda 2796 \text{ \AA}$  equivalent width versus  $\log N(\text{H I})$  for DLAs in the Magellan sample that contained spectral coverage of the MgII  $\lambda 2796 \text{ \AA}$  line. Red squares denote the high redshift points, while blue circles represent the low redshift points, where the sample was split on the median redshift,  $z_{\text{abs}}=2.44$ .

## 6 CONCLUSIONS

We present the first uniformly selected DLA sample with medium-resolution (or higher) measurements of metallicity,  $\Delta v_{90}$  and  $W_{\lambda 1526}$ . This sample is unique in the sense that it was created *a priori* to be as unbiased as possible by including all SDSS DR5 DLAs visible from the Magellan site, without regard to metallicity,  $\log N_{\text{HI}}$ , or any other DLA property. Only 2 constraints limited the sample: 1) a lower redshift cutoff of  $z_{\text{abs}} = 2.2$  such that the systems could be searched for  $\text{H}_2$ , and 2) a magnitude cut of  $i \leq 19$

such that the sample could be observed in a reasonable amount of time. While the initial motivation for this survey was to determine the true covering factor and fraction of H<sub>2</sub> in DLAs – the results of which we present in a second paper (Jorgenson et al. 2013) – we summarize here the major results of this current paper as follows:

(i) Using spectra primarily taken with the medium-resolution Magellan/MagE spectrograph, we measure the  $\log N_{\text{HI}}$ ,  $[M/H]$ ,  $[\text{Fe}/H]$ ,  $\Delta v_{90}$ ,  $W_{\lambda 1526}$ ,  $W_{\lambda 1548}$  and  $W_{\lambda 2796}$  of a sample of 99 uniformly selected DLAs.

(ii) The potential underestimation of metallicity due to possible undetected saturation of spectral features in medium-resolution spectra is determined to be mostly alleviated by applying a flux-based saturation criterion of  $F_{\text{min}}/F_q < 0.65$ . Simulations and tests show that the application of this criterion likely alleviates the worst cases, and any additional underestimation in the metal-line column density will likely be less than  $\sim 0.3$  dex.

(iii) We determine the redshift evolution in the cosmic mean metallicity over the redshift range,  $z = [2.2, 4.4]$  (but note that the majority of DLAs fall between  $z = [2.2, 3.5]$ ), to be  $\langle Z \rangle = (-0.04 \pm 0.13)z - (1.06 \pm 0.36)$ , an evolution that is somewhat flatter than that found by previous works such as R12, who measure an evolution described by  $\langle Z \rangle = (-0.22 \pm 0.03)z - (0.65 \pm 0.09)$  over  $z \in [0, 5.5]$ . Strictly speaking, these slopes are consistent with each other at the  $2\sigma$  level.

(iv) A simple separation of the sample into low and high redshift bins reveals very little evolution in any of the DLA parameters, including  $\Delta v_{90}$  and the equivalent width of the Si II  $\lambda 1526$  transition,  $W_{\lambda 1526}$ , contrary to the results of Ledoux et al. (2006).

(v) We find a highly significant correlation,  $>9\sigma$ , between  $W_{\lambda 1526}$  and metallicity, similar to that found by Prochaska et al. (2008).  $W_{\lambda 1526}$  and the equivalent width of the high-ion gas tracer, C IV  $\lambda 1548\text{\AA}$ ,  $W_{\lambda 1548}$ , are also correlated at the  $>5.5\sigma$  level. And similar to the results of Murphy et al. (2007), we find a correlation between the equivalent width of Mg II  $\lambda 2796$ ,  $W_{\lambda 2796}$ , and metallicity at the level of  $2.5\sigma$ .

Initially, the most striking result of the work presented in this paper is the somewhat flatter slope – consistent with zero – derived for the evolution of the cosmic mean metallicity. Using this result alone, which is based on the only uniformly selected sample in the literature, we do not see significant evidence for metallicity evolution in DLAs in the redshift range  $z = 2.2 - 4.4$ . The significant evolution found by R12, is heavily weighted by the low and high redshift ends of their sample. These facts lead us to the conclusion that the evolution of cosmic mean metallicity over the redshift range  $z = 2.2 - 4.4$  may be flatter than that found by R12 and closer to the value presented here. However, we emphasize that our result is strictly consistent with that of R12. Logically, the evolution in DLA metallicity across cosmic time is expected if models of galaxy formation and evolution and the role played by DLAs in that evolution are correct. In this paradigm, the non-evolution found in the Magellan survey stands out as contradictory. However, given the limited redshift range and size of the Magellan survey, we caution that, while intriguing, this result is difficult to interpret in the context of the broader cosmological picture without additional unbiased data (or at least data with a well-understood, correctable selection function) including, crucially, both the high ( $z \gg 4$ ) and low ( $z \ll 2$ ) redshift regimes.

## ACKNOWLEDGEMENTS

R. A. J. gratefully acknowledges support from the STFC-funded Galaxy Formation and Evolution programme at the Institute of Astronomy, University of Cambridge and the NSF Astronomy and Astrophysics Postdoctoral Fellowship under award AST-1102683. M. T. M. thanks the Australian Research Council for a QEII Research Fellowship (DP0877998) and Discovery Project grant (DP130100568). The authors thank M. Rafelski for sharing data prior to publication. Australian access to the Magellan Telescopes was supported through the Major National Research Facilities program and National Collaborative Research Infrastructure Strategy of the Australian Federal Government.

## REFERENCES

- Asplund M., Grevesse N., Sauval A. J., Scott P., 2009, *ARAA*, 47, 481  
 Cen R., 2012, *ApJ*, 748, 121  
 Cooke R., Pettini M., Steidel C. C., Rudie G. C., Jorgenson R. A., 2011, *MNRAS*, 412, 1047  
 Davé R., Oppenheimer B. D., Finlator K., 2011, *MNRAS*, 415, 11  
 Dekker H., D’Odorico S., Kaufer A., Delabre B., Kotzłowski H., 2000, in *Society of Photo-Optical Instrumentation Engineers (SPIE) Conference Series*, Vol. 4008, *Society of Photo-Optical Instrumentation Engineers (SPIE) Conference Series*, M. Iye & A. F. Moorwood, ed., pp. 534–545  
 D’Odorico S. et al., 2004, in *Society of Photo-Optical Instrumentation Engineers (SPIE) Conference Series*, Vol. 5492, *Society of Photo-Optical Instrumentation Engineers (SPIE) Conference Series*, A. F. M. Moorwood & M. Iye, ed., pp. 220–229  
 Ellison S. L., Yan L., Hook I. M., Pettini M., Wall J. V., Shaver P., 2001, *A & A*, 379, 393  
 Frank S., Péroux C., 2010, *MNRAS*, 406, 2235  
 Fumagalli M., Prochaska J. X., Kasen D., Dekel A., Ceverino D., Primack J. R., 2011, *MNRAS*, 418, 1796  
 Haehnelt M. G., Steinmetz M., Rauch M., 1998, *ApJ*, 495, 647  
 Herbert-Fort S., Prochaska J. X., Dessauges-Zavadsky M., Ellison S. L., Howk J. C., Wolfe A. M., Prochter G. E., 2006, *PASP*, 118, 1077  
 Jorgenson R. A., Murphy M., Thompson R., Carswell R. F., 2013, *MNRAS*  
 Jorgenson R. A., Wolfe A. M., Prochaska J. X., Lu L., Howk J. C., Cooke J., Gawiser E., Gelino D. M., 2006, *ApJ*, 646, 730  
 Khare P., vanden Berk D., York D. G., Lundgren B., Kulkarni V. P., 2012, *MNRAS*, 419, 1028  
 Kulkarni V. P., Fall S. M., Lauroesch J. T., York D. G., Welty D. E., Khare P., Truran J. W., 2005, *ApJ*, 618, 68  
 Kulkarni V. P., Khare P., Péroux C., York D. G., Lauroesch J. T., Meiring J. D., 2007, *ApJ*, 661, 88  
 Kulkarni V. P., Khare P., Som D., Meiring J., York D. G., Péroux C., Lauroesch J. T., 2010, *New Astron.*, 15, 735  
 Lanzetta K. M., Wolfe A. M., Turnshek D. A., 1995, *ApJ*, 440, 435  
 Ledoux C., Petitjean P., Fynbo J. P. U., Møller P., Srianand R., 2006, *A & A*, 457, 71  
 Maller A. H., Prochaska J. X., Somerville R. S., Primack J. R., 2003, *MNRAS*, 343, 268  
 Marshall J. L. et al., 2008, in *Society of Photo-Optical Instrumentation Engineers (SPIE) Conference Series*, Vol. 7014, *Society of Photo-Optical Instrumentation Engineers (SPIE) Conference Series*  
 Murphy M. T., Curran S. J., Webb J. K., Ménager H., Zych B. J., 2007, *MNRAS*, 376, 673  
 Murphy M. T., Liske J., 2004, *MNRAS*, 354, L31  
 Noterdaeme P., Petitjean P., Ledoux C., Srianand R., 2009, *A & A*, 505, 1087  
 Penprase B. E., Prochaska J. X., Sargent W. L. W., Toro-Martinez I., Beeler D. J., 2010, *ApJ*, 721, 1  
 Pettini M., Ellison S. L., Steidel C. C., Bowen D. V., 1999, *ApJ*, 510, 576

- Prochaska J. X., Chen H.-W., Wolfe A. M., Dessauges-Zavadsky M., Bloom J. S., 2008, *ApJ*, 672, 59
- Prochaska J. X., Gawiser E., Wolfe A. M., Castro S., Djorgovski S. G., 2003a, *ApJL*, 595, L9
- Prochaska J. X., Gawiser E., Wolfe A. M., Cooke J., Gelino D., 2003b, *ApJS*, 147, 227
- Prochaska J. X., Herbert-Fort S., Wolfe A. M., 2005, *ApJ*, 635, 123
- Prochaska J. X., Wolfe A. M., 1997, *ApJ*, 487, 73
- Prochaska J. X., Wolfe A. M., 2009, *ApJ*, 696, 1543
- Rafelski M., Wolfe A. M., Prochaska J. X., Neeleman M., Mendez A. J., 2012, *ApJ*, 755, 89
- Richards G. T. et al., 2001, *AJ*, 121, 2308
- Savage B. D., Sembach K. R., 1991, *ApJ*, 379, 245
- Vladilo G., 2002, *A & A*, 391, 407
- Vladilo G., Bonifacio P., Centurión M., Molaro P., 2000, *ApJ*, 543, 24
- Vladilo G., Prochaska J. X., Wolfe A. M., 2008, *A & A*, 478, 701
- Vogt S. S. et al., 1994, in *Society of Photo-Optical Instrumentation Engineers (SPIE) Conference Series*, Vol. 2198, *Society of Photo-Optical Instrumentation Engineers (SPIE) Conference Series*, D. L. Crawford & E. R. Craine, ed., p. 362
- Wolfe A. M., Gawiser E., Prochaska J. X., 2005, *ARAA*, 43, 861
- Wolfe A. M., Prochaska J. X., 2000, *ApJ*, 545, 603
- Worseck G., Prochaska J. X., 2011, *ApJ*, 728, 23